



HAL
open science

Timing and Provenance of Volcanic Fluxes Around the Permian-Triassic Boundary Mass Extinction in South China: U-Pb Zircon Geochronology, Volcanic Ash Geochemistry and Mercury Isotopes

Oluwaseun Edward, André Navin Paul, Hugo Bucher, Christian Vérard, Thierry Adatte, Jeroen E. Sonke, Urs Schaltegger, Torsten Vennemann

► To cite this version:

Oluwaseun Edward, André Navin Paul, Hugo Bucher, Christian Vérard, Thierry Adatte, et al.. Timing and Provenance of Volcanic Fluxes Around the Permian-Triassic Boundary Mass Extinction in South China: U-Pb Zircon Geochronology, Volcanic Ash Geochemistry and Mercury Isotopes. *Geochemistry, Geophysics, Geosystems*, 2023, 24, 10.1029/2023GC010912 . insu-04198441

HAL Id: insu-04198441

<https://insu.hal.science/insu-04198441v1>

Submitted on 7 Sep 2023

HAL is a multi-disciplinary open access archive for the deposit and dissemination of scientific research documents, whether they are published or not. The documents may come from teaching and research institutions in France or abroad, or from public or private research centers.

L'archive ouverte pluridisciplinaire **HAL**, est destinée au dépôt et à la diffusion de documents scientifiques de niveau recherche, publiés ou non, émanant des établissements d'enseignement et de recherche français ou étrangers, des laboratoires publics ou privés.



Distributed under a Creative Commons Attribution - NonCommercial - NoDerivatives 4.0 International License

Geochemistry, Geophysics, Geosystems®



RESEARCH ARTICLE

10.1029/2023GC010912

Key Points:

- Mercury concentrations show elevated volcanic fluxes to South China before and after the Permian-Triassic boundary (PTB)
- The recorded mercury anomalies are attributed primarily to regional subduction-related arc volcanism, not the Siberian Traps
- Mercury anomalies close to the PTB are not a reliable stratigraphic marker for the mass extinction event

Supporting Information:

Supporting Information may be found in the online version of this article.

Correspondence to:

O. Edward,
oluwaseun.edward@unil.ch

Citation:

Edward, O., Paul, A. N., Bucher, H., V  rard, C., Adatte, T., Sonke, J. E., et al. (2023). Timing and provenance of volcanic fluxes around the Permian-Triassic boundary mass extinction in South China: U-Pb zircon geochronology, volcanic ash geochemistry and mercury isotopes. *Geochemistry, Geophysics, Geosystems*, 24, e2023GC010912. <https://doi.org/10.1029/2023GC010912>

Received 14 FEB 2023

Accepted 23 MAY 2023

Author Contributions:

Conceptualization: Oluwaseun Edward, Hugo Bucher, Urs Schaltegger, Torsten Vennemann

Data curation: Oluwaseun Edward, Jeroen E. Sonke

Formal analysis: Oluwaseun Edward, Andr   Navin Paul, Christian V  rard

Timing and Provenance of Volcanic Fluxes Around the Permian-Triassic Boundary Mass Extinction in South China: U-Pb Zircon Geochronology, Volcanic Ash Geochemistry and Mercury Isotopes

Oluwaseun Edward¹ , Andr   Navin Paul² , Hugo Bucher³, Christian V  rard² , Thierry Adatte⁴, Jeroen E. Sonke⁵ , Urs Schaltegger², and Torsten Vennemann¹ 

¹Institute of Earth Surface Dynamics, G  opolis, University of Lausanne, Lausanne, Switzerland, ²Department of Earth Sciences, Universit   de Gen  ve, Gen  ve, Switzerland, ³Pal  ontologisches Institut der Universit  t Z  rich, Z  rich, Switzerland, ⁴Institute of Earth Sciences, G  opolis, University of Lausanne, Lausanne, Switzerland, ⁵Observatoire Midi-Pyr  n  es, G  osciences Environnement Toulouse, Universit   Paul Sabatier Toulouse 3, Toulouse, France

Abstract Anomalous mercury (Hg) contents recorded near the Permian-Triassic boundary (PTB) are often linked to Siberian Traps Large Igneous Province (STLIP) volcanism and the Permian-Triassic boundary mass extinction (PTBME). However, mounting evidence indicates that the relation between STLIP volcanism and Hg “anomalies” is not straightforward. This study focuses on the timing and provenance of volcanic fluxes around the PTBME in South China. We constrain carbon isotope ($\delta^{13}\text{C}$) and Hg concentration and isotope records by utilizing high-precision U-Pb zircon ages from two expanded deep-water marine sections spanning the Late Permian to Early Triassic in the Nanpanjiang Basin. Results reveal two episodes of Hg enrichment. The oldest episode predates the onset of a large negative $\delta^{13}\text{C}$ excursion, which is documented to be older than 252.07 ± 0.130 Ma. The second episode occurred between 251.822 ± 0.060 and 251.589 ± 0.062 Ma, coinciding with the nadir of the $\delta^{13}\text{C}$ excursion. Volcanic ash geochemistry and Hg isotope compositions suggest that mercury was mainly sourced from subduction-related volcanic arc magmatism in the Tethys region, which peaked between 251.668 ± 0.079 and 251.589 ± 0.052 Ma. These results are compatible with suggestions that regional arc volcanism contributed to the causes of the PTBME in South China and provide evidence that Hg anomalies close to the PTB are not a reliable stratigraphic marker for the PTB extinction event. This study demonstrates that relations between volcanism, environmental perturbations and mass extinction during the Permian-Triassic transition are better resolved with the aid of high-precision U-Pb zircon ages.

Plain Language Summary Unusually high mercury contents in sedimentary rock sequences and the mass extinction of organisms during the transition from the Permian-Triassic Period are often linked to Siberian Traps volcanism. However, results from several studies indicate that the relationship between this massive volcanism and mercury peaks in Permian- to Triassic-aged rocks in the South China region is complex. This study combines the geochemical and isotopic records of carbon and mercury from Late Permian to Early Triassic sedimentary rocks, with absolute ages determined from interlayered volcanic ashes, to investigate the presence, timing, and source of volcanic inputs to these rock successions in South China. Results show higher mercury concentrations in two intervals, one before and after the Permian-Triassic boundary (PTB). Absolute age results indicate that the mercury peak closest to the PTB occurred around 300,000 years after the mass extinction. We attribute the mercury peaks to more local volcanic activity than the far away Siberian Traps and suggest that this regional-scale volcanic activity began shortly before 252 million years ago (Ma) and peaked around 251.6 Ma.

1. Introduction

The Paleozoic-Mesozoic transition (ca. 252 million years ago) was characterized by the largest mass extinction event in the Phanerozoic—the Permian-Triassic boundary mass extinction (PTBME) (Erwin, 1998; Stanley, 2016). This event paved the way for the faunal transition from the Paleozoic evolutionary fauna to the modern fauna (Dal Corso et al., 2022). Furthermore, major perturbations of the global carbon and mercury cycles (expressed as negative carbon (C) isotope excursions and mercury (Hg) concentration spikes, respectively) are

   2023 The Authors. *Geochemistry, Geophysics, Geosystems* published by Wiley Periodicals LLC on behalf of American Geophysical Union.

This is an open access article under the terms of the [Creative Commons Attribution-NonCommercial License](https://creativecommons.org/licenses/by-nc/4.0/), which permits use, distribution and reproduction in any medium, provided the original work is properly cited and is not used for commercial purposes.

Funding acquisition: Hugo Bucher, Urs Schaltegger, Torsten Vennemann

Investigation: Oluwaseun Edward, André Navin Paul, Hugo Bucher, Thierry Adatte, Jeroen E. Sonke

Methodology: Oluwaseun Edward, André Navin Paul, Hugo Bucher, Urs Schaltegger

Project Administration: Hugo Bucher, Urs Schaltegger, Torsten Vennemann

Resources: Thierry Adatte, Jeroen E. Sonke, Urs Schaltegger, Torsten Vennemann

Supervision: Hugo Bucher, Torsten Vennemann

Validation: Christian Vérard, Urs Schaltegger, Torsten Vennemann

Visualization: Oluwaseun Edward, André Navin Paul, Christian Vérard

Writing – original draft: Oluwaseun Edward, André Navin Paul

Writing – review & editing: Oluwaseun Edward, André Navin Paul, Hugo Bucher, Christian Vérard, Thierry Adatte, Jeroen E. Sonke, Urs Schaltegger, Torsten Vennemann

documented for sedimentary successions straddling the Permian-Triassic boundary (PTB) in several spatially disparate localities (e.g., Baud et al., 1989, 1996; Grasby et al., 2013; Korte & Kozur, 2010; Sanei et al., 2012; S. Z. Shen, Cao, et al., 2013; J. Shen, Chen, et al., 2019; Sial et al., 2020). Causal mechanisms for the extinction are still debated. However, the most popular trigger suggested by researchers is volcanic activity of the Siberian Large Igneous Province (LIP) (Siberian Traps Large Igneous Province, STLIP), based on a temporal overlap between U-Pb ages of STLIP rocks and those of volcanic ash beds in the Meishan Global Stratotype Section and Point (GSSP) (Burgess & Bowring, 2015; Burgess et al., 2017).

The connection between volcanic activity and Hg concentration spikes in sedimentary successions is founded on the understanding that volcanoes are a dominant natural source of Hg to the environment (Pyle & Mather, 2003). As such, LIP volcanism could result in the emission and sequestration of high levels of Hg in the environment. Consequently, mercury “anomalies”—relatively high Hg concentrations or Hg/total organic carbon (TOC) ratios in a portion of strata within a given sedimentary succession—are used to trace the timing of LIP magmatism in the geological record (Grasby et al., 2019; Percival et al., 2021; Yager et al., 2021). In the case of the $\delta^{13}\text{C}$ record, previous studies have interpreted the negative C isotope excursion associated with the PTB as the result of the intrusion of magma into surrounding organic-rich country rocks (e.g., coal, shale) and petroleum-rich evaporites in the Tunguska Basin, Siberia (Broadley et al., 2018; Payne & Kump, 2007; H. Svensen et al., 2009). Thus, Hg anomalies and negative $\delta^{13}\text{C}$ excursions recorded close to the PTB are usually interpreted in the context of STLIP volcanism and its associated deleterious environmental effects leading to faunal extinction.

However, our understanding of the links between STLIP volcanism, carbon cycle perturbations and mass extinction during the Permian-Triassic (P-T) transition is still complicated by several factors. First, Hg and Hg/TOC content vary significantly near the PTB between different localities and the relative timing of Hg anomalies with regard to the PTBME horizon is inconsistent (e.g., J. Shen, Chen, et al., 2019; Sial et al., 2020; X. D. Wang et al., 2018). In addition, Hg anomalies can also be influenced by factors other than direct volcanic emissions. For instance, Hg anomalies can arise from increased input of Hg remobilized from soils to marine sediments due to increased erosion and continental weathering rates (Them et al., 2019), as well as enhanced sequestration by sulfides in euxinic depositional environments (J. Shen et al., 2020). In addition, sedimentary Hg records can be distorted by post-depositional weathering, erosion, and thermal alteration (Charbonnier et al., 2020; D. Chen et al., 2022). Second, the correlation of geochemical records between different localities is fraught with uncertainty because the position of the PTB in many successions remains uncertain (e.g., Johnson et al., 2021; J. Shen, Chen, et al., 2019; Sial et al., 2020). Also, sedimentary and volcanic successions straddling the Permian and Triassic are often characterized by an unconformity at the PTB (Burgess & Bowring, 2015; Davydov, 2021; H. Yin et al., 2014), which for South China has been estimated to represent a time gap of about 89 ± 38 kyr for the Permian part (Baresel, Bucher, Bagherpour, et al., 2017). Third, it has become apparent that several paleocontinents, including South China, experienced extensive regional intermediate to felsic volcanism during the P-T transition (Gao et al., 2013; J. Shen et al., 2021; Vajda et al., 2020; H. Yin et al., 1992; H. Zhang, Zhang, & Shen, 2021), increasing the potential sources of volcanic Hg input to PTB marine records at these localities. Fourth, absolute time calibration of the eruptive history of the STLIP remains coarse, limiting precise temporal correlations between STLIP magmatism and mass extinction (Dal Corso et al., 2022), although, U-Pb geochronologic evidence suggests that the PTBME may have been limited to only a short period of STLIP magmatism (Burgess et al., 2017). Consequently, considering the complex biogeochemical cycling of Hg, the widespread incompleteness of the PTB rock record (which limits the accuracy of chemostratigraphic and biostratigraphic correlations and the placement of the PTB), and the occurrence of more proximal regional volcanic activity capable of locally supplying Hg, links between Hg anomalies around the PTB and STLIP magmatism cannot be unequivocally inferred without a thorough assessment of the provenance of the recorded Hg anomalies and their timing relative to the PTBME using precise and accurate geochronology.

Hg isotopes are widely used to trace the sources of Hg anomalies in ancient sedimentary successions as different transformations during the biogeochemical cycling of Hg can induce mass-dependent (MDF) and/or mass-independent fractionation (MIF) of Hg isotopes (Blum et al., 2014; Thibodeau & Bergquist, 2017). Previous studies have applied Hg isotopes in investigating the source of Hg anomalies and its relationship to the PTBME in P-T successions of South China and elsewhere (Grasby et al., 2017; J. Shen, Chen, et al., 2019; J. Shen et al., 2021; X. D. Wang et al., 2018; X. Wang, Cawood, Zhao, Zhao, et al., 2019). However, these studies have provided mixed results, with Hg MIF data from nearshore depositional settings reflecting a dominant terrestrial Hg source and those from deeper-water depositional settings being congruent with atmospheric volcanic Hg

input (Grasby et al., 2017; J. Shen et al., 2023; X. D. Wang et al., 2018). Hence, it has been suggested that the Hg isotope record for these successions mostly reflects their depositional setting (Yager et al., 2021) and that distal/deep-water marine sections, being less vulnerable to terrestrial Hg inputs, may be better suited for investigations of volcanic Hg input sources (Grasby et al., 2017; Thibodeau & Bergquist, 2017; X. D. Wang et al., 2018).

The Upper Permian to Lower Triassic of South China is characterized by the widespread occurrence of volcanic ash layers (Gao et al., 2013; He et al., 2014; Yang et al., 2012; H. Yin et al., 1992), permitting precise and accurate U-Pb zircon geochronological calibrations of P-T successions (e.g., Baresel, Bucher, Bagherpour, et al., 2017; Baresel, Bucher, Brosse, et al., 2017; Burgess et al., 2014; Lehrmann et al., 2015; S. Z. Shen, Ramezani, et al., 2019), as well as providing a means of evaluating the provenance of volcanic products (e.g., zircon) to sedimentary successions in South China (e.g., Jiao et al., 2022; T. Y. Zhao et al., 2019). However, except for the Shangsi section (with published U-Pb zircon ages, S. Shen et al., 2011), Hg anomalies recorded near the PTB from deep-water marine successions in South China (e.g., J. Shen, Chen, et al., 2019; X. D. Wang et al., 2018) lack U-Pb zircon age calibration. Also, the published U-Pb zircon ages for Shangsi were not obtained with the most recent EARTHTIME spike (S. Z. Shen et al., 2011; Yuan et al., 2019), which makes a direct comparison with ages obtained using this spike problematic at high temporal resolution. To accurately account for spike composition effects on the weighted mean U-Pb age when comparing ages determined using different spikes, the tracer and analytical uncertainty needs to be propagated (i.e., Y uncertainty, see Section 2.5, not reported in S. Z. Shen et al. (2011)). This Y uncertainty propagation results in less-precise ages, inhibiting age comparison at high temporal resolution. In addition to enabling precise geochronology, volcanic ashes provide an archive for the assessment of magmatic sources, as their geochemical compositions reflect those of the source magma (e.g., He et al., 2014; Q. Song et al., 2022; Yang et al., 2012). This study presents, for the first time, a paired $\delta^{13}\text{C}$ and Hg (concentration and isotope) record calibrated by precise and accurate U-Pb zircon ages from two sections (Laxian and Potuo) representing deep-water marine depositional environments in the Nanpanjiang Basin, South China. The aim of the study is to assess the occurrence, timing and provenance of volcanic fluxes during the P-T transition in South China.

1.1. Geological Context

The Potuo and Laxian sections (Figure 1) are situated in the NE-SW trending Pingtang syncline, which in the present-day is located in the northern part of the Nanpanjiang Basin, South China (Bagherpour et al., 2020). The Changhsingian (Late Permian) sedimentary succession in Potuo is characterized by thin-bedded siliceous mudstones interbedded with volcanic ash layers: the Talung/Dalong Formation (Bagherpour et al., 2020; Baresel, Bucher, Brosse, et al., 2017). The Griesbachian (Induan, Early Triassic) consists of laminated black shales with interbedded concretionary micritic limestones and occasional ash beds representing the Daye/Ziyun Formation (Bagherpour et al., 2020). The Changhsingian to Griesbachian sedimentary succession for Laxian is similar to that of Potuo except that there are no concretionary micritic limestone beds interbedded with the Griesbachian shale units (Bagherpour et al., 2020). The Late Permian to Early Triassic sedimentary sequence in these localities is interpreted to have been deposited as a continuous section in a deep-water basin paleoenvironment (Bagherpour et al., 2020). Furthermore, there is no field evidence for an unconformity between the Talung and Daye formations in Laxian, consistent with similar observations for other sections in the Nanpanjiang Basin (Bagherpour et al., 2020; Baresel, Bucher, Brosse, et al., 2017; Dai et al., 2019). In addition, the presence of volcanic ashes in these sections enables studies of the latest Permian to earliest Triassic volcanic fluxes to the Nanpanjiang Basin of South China. As such, these sections are ideally suited for our combined geochronologic and geochemical study, having been deposited in troughs within a horst-and-graben paleotopography (Bagherpour et al., 2020). Samples spanning the Upper Permian to Lower Triassic used for this study are the same as those analyzed by Bagherpour et al. (2020) and details on the geological setting, lithostratigraphy, biostratigraphy, as well as $\delta^{13}\text{C}$ record for these sections are given in that study. A sampling gap between upper Changhsingian to lower Griesbachian strata hinders the documentation of a continuous Upper Permian to Lower Triassic record for Potuo (Bagherpour et al., 2020). Nevertheless, the combination of geochemical data with high-precision U-Pb zircon ages from both sections makes geochemical records from these sections valuable.

2. Materials and Methods

For this study, measurements of the Hg concentrations ($n = 70$) and isotopic compositions ($n = 22$), TOC contents ($n = 60$), and major and trace element concentrations for sedimentary rocks and interbedded volcanic ash beds

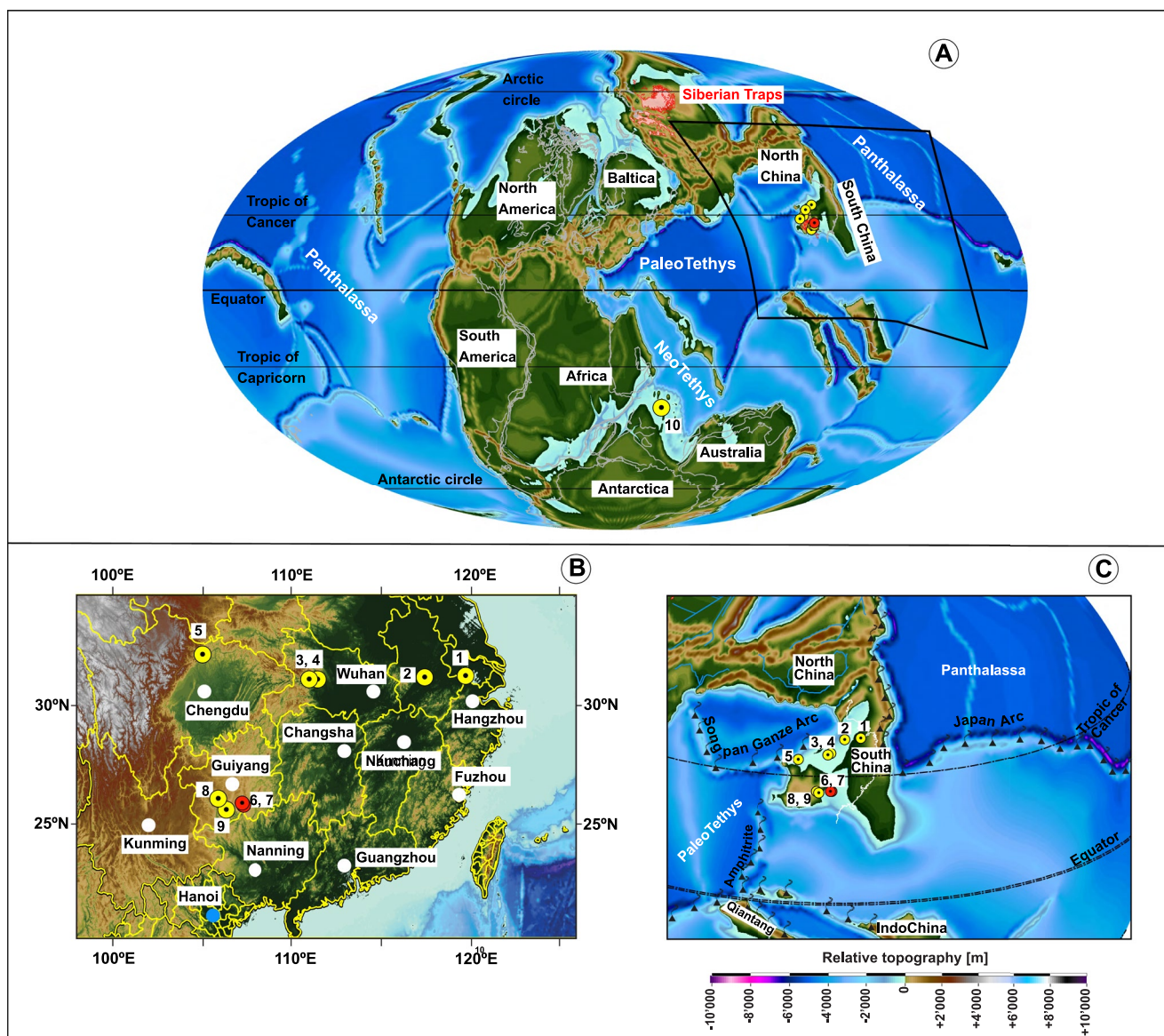


Figure 1. Maps showing the location of the studied successions, as well as other marine successions in the Tethys region from which Permian-Triassic (P–T) transition mercury records have been published. (a) Global paleogeographic map at the P–T transition after the Panalasia model (Vérard, 2019). Locality marked “10” represents the paleo-location of Guryul Ravine, northern India. (b) Map showing the present-day location of the studied sections (red circles) and other deep-water marine sections in South China (yellow circles); white circles show the main cities. The sections are represented by numbers as follows: 1, Meishan; 2, Majiashan; 3, Daxiakou; 4, Xiakou; 5, Shangsi; 6, Laxian; 7, Potuo; 8, Xinmin; 9, Kejiao. (c) Detailed map of the South China area (orthogonal projection) with the paleo-location of the discussed sections.

($n = 55$) were made. These data are complemented by U–Pb zircon geochronology based on single zircon grains from five volcanic ash beds in the two sections (Table S1 in Supporting Information S1).

2.1. Stratigraphical Correlation of the Study Sections

Stratigraphical correlation between the two sections studied—Laxian (25.78880°N, 107.29750°E) and Potuo (25.82638°N, 107.24861°E), follows Bagherpour et al. (2020). The PTB is delineated based on the lithostratigraphic boundary between the Talung and Daye formations, which for deep-water sections of the Nanpanjiang Basin has been shown to be equivalent to the PTB as defined at the Meishan D GSSP based on U–Pb zircon ages (Baresel, Bucher, Brosse, et al., 2017; Burgess et al., 2014). Furthermore, the transition from the Talung/Dalong Fm. to Daye Fm. is considered to correspond to the mass extinction interval in the Nanpanjiang Basin (J. Shen, Chen,

et al., 2019). The stratigraphical correlation of the Laxian and Potuo sections, which is based on lithostratigraphy (Bagherpour et al., 2020), is congruent with the similarity of the Hg trends for Potuo and Laxian and is consistent with our new U-Pb zircon ages (see Section 3).

2.2. Mercury Concentration and Isotopic Composition

Mercury concentration was measured using a Zeeman R-915F high-frequency atomic absorption spectrometer at the University of Lausanne, Switzerland. Samples (sedimentary rocks, including volcanic ashes) were analyzed in triplicates to ensure analytical precision and the reference material—GSD-11, Chinese alluvium (Hg concentration of 72 ± 9 ppb; Zintwana et al., 2012) was used to monitor the accuracy of the measurements (correlation coefficient = 0.99, standard residual deviation = 5%).

Twenty-two samples (Potuo = 11, Laxian = 11) with sufficiently high Hg concentrations (≥ 9 ppb) were selected for Hg isotopic analysis at the Observatoire Midi-Pyrénées, Toulouse, France. Mercury was preconcentrated using a double-stage tube furnace—acid-trapping protocol as detailed by R. Sun et al. (2013). Powdered samples were loaded in quartz tubes (pre-cleaned at 550°C), capped at both ends with quartz wool and heated in a combustion furnace connected to a flow of Hg-free oxygen and set to ramp up from room temperature to 900°C within 6 hr. Liberated gaseous Hg⁰ was then purged into a decomposition oven, held at 1,000°C, using a continuous flow of oxygen. Subsequently, the Hg⁰ was collected by oxidation to Hg^{II} in a trapping solution of 40% (v/v) inverse aqua regia (iAR, 2HNO₃/1HCl), which was then diluted at the end of the 6 hr pre-concentration to 20% (v/v) iAR and stored at 4°C in the dark before Hg isotopic measurements (R. Sun et al., 2013). Two certified reference materials, NIST 1632D (bituminous coal, $n = 2$) and MESS3 (Arctic marine sediment, $n = 2$) were processed along with the samples. Hg isotope compositions were subsequently measured in duplicate over two analytical sessions by cold vapor multi-collector inductively coupled plasma mass spectrometry (CV-MC-ICP-MS) following analytical procedures detailed by Sonke et al. (2010), R. Sun et al. (2013), and Jiskra et al. (2021). Briefly, the Hg^{II} in the iAR trap solution was reduced to Hg⁰ vapor using SnCl₂ solution (3%, w/v, in 1 M HCl) and then analyzed for Hg stable isotopes using an online CETAC HGX-200 cold vapor generator coupled to a Thermo-Scientific Neptune PLUS™ equipped with a 10¹² Ω resistor on the ¹⁹⁸Hg isotope. The MC-ICP-MS instrumental mass bias was corrected by sample-standard bracketing using the NIST 3133 standard at matching standard and sample concentrations (0.71 and 2.1 ppb). Long-term instrumental precision was monitored by repeated analysis of the ETH-Fluka ($n = 6$) and UM-Almaden ($n = 3$) Hg standard solutions at Hg concentrations corresponding to the samples (i.e., 0.71 and 2.1 ng/g). Procedural blanks had an average Hg concentration of ~0.01 ng/g ($n = 3$). MDF of Hg isotopes is reported in small delta notation (δ) as $\delta^{202}\text{Hg}$ in permil (‰) relative to the bracketing NIST 3133 standard:

$$\delta^{202}\text{Hg} = \left[\left(\frac{{}^{202}\text{Hg}/{}^{198}\text{Hg}}{\text{sample}} / \left(\frac{{}^{202}\text{Hg}/{}^{202}\text{Hg}}{\text{NIST3133}} - 1 \right) \times 10^3 \right] \quad (1)$$

Mass independent fractionation (MIF) values are denoted using capital delta (Δ) notation and are defined as the difference between the measured values of $\delta^{199}\text{Hg}$, $\delta^{200}\text{Hg}$, $\delta^{201}\text{Hg}$, $\delta^{204}\text{Hg}$, and those predicted for MDF with respect to $\delta^{202}\text{Hg}$ using the kinetic MDF law as follows:

$$\Delta^{\text{xxx}}\text{Hg} = \delta^{\text{xxx}}\text{Hg} - K_{\text{xxx}} \times \delta^{202}\text{Hg} \quad (2)$$

where xxx refers to Hg isotope masses 199, 200, 201, and 204, and K_{xxx} refers to the constants that are used to calculate values for $\Delta^{\text{xxx}}\text{Hg}$, which are 0.2520, 0.5024, 0.7520, and 1.4930 for $\delta^{199}\text{Hg}$, $\delta^{200}\text{Hg}$, $\delta^{201}\text{Hg}$, and $\delta^{204}\text{Hg}$ respectively (Blum & Bergquist, 2007). Hg isotopic compositions are reported as the mean of duplicate measurements and analytical uncertainty of isotopic analysis are reported conservatively, as either the 2σ ($2 \times$ standard deviation) of the replicate sample measurements or that of the standard with the largest 2σ , whichever was larger. ETH-Fluka and UM-Almaden standard solutions yielded mean values ($\pm 2\sigma$) of $-1.48 \pm 0.14\text{‰}$, $0.09 \pm 0.03\text{‰}$, $0.04 \pm 0.03\text{‰}$, $0.04 \pm 0.07\text{‰}$; and $-0.59 \pm 0.09\text{‰}$, $-0.03 \pm 0.10\text{‰}$, $0.02 \pm 0.06\text{‰}$, and $-0.05 \pm 0.07\text{‰}$ for $\delta^{202}\text{Hg}$, $\Delta^{199}\text{Hg}$, $\Delta^{200}\text{Hg}$, and $\Delta^{201}\text{Hg}$ respectively. NIST 1632D and MESS-3 had mean values of $-1.93 \pm 0.32\text{‰}$, $-0.01 \pm 0.05\text{‰}$, $-0.06 \pm 0.08\text{‰}$, $-0.06 \pm 0.01\text{‰}$; and $-2.25 \pm 0.02\text{‰}$, $0 \pm 0.04\text{‰}$, $0.04 \pm 0.03\text{‰}$, and $-0.14 \pm 0.14\text{‰}$ for $\delta^{202}\text{Hg}$, $\Delta^{199}\text{Hg}$, $\Delta^{200}\text{Hg}$, and $\Delta^{201}\text{Hg}$ respectively. These mean values are comparable with reported values for these standard solutions and certified reference materials (Jiskra et al., 2019; Kwon et al., 2015; R. Sun et al., 2013).

2.3. Organic Carbon Content

All TOC content data for Laxian ($n = 26$) were acquired during the present study. For the Potuo section, 10 data points are from Bagherpour et al. (2020) and an additional 28 samples have been analyzed for this study. Organic matter (OM) content and preservation were assessed by Rock-Eval pyrolysis using a Rock Eval™ 6 with the analytical procedures described by Behar et al. (2001). This included measurements of TOC content, pyrolysis temperature (T_{\max}), hydrogen index (HI) and oxygen index (OI). The standard IFP160000 was used for calibration of the samples and instrumental precision was about 0.1 wt.% for TOC, 10 mg HC/g for HI and 10 mg CO₂/g for OI.

2.4. Major and Trace Element Analysis

Major and trace element concentrations were analyzed by X-ray fluorescence (XRF) spectrometry on glass discs and pressed tablets, respectively, using a PANalytical PW2400 XRF spectrometer at the University of Lausanne, Switzerland. The standard reference materials: JLS-1, JDO-1, and BHVO were used for the assessment of analytical accuracy. External reproducibility (1σ) is between 0.5% and 5% depending on the element, and detection limit for major elements is ca. 0.01% and between 1 and 7 ppm for trace elements.

2.5. U-Pb Zircon Geochronology

In total, nine volcanic ash layers from the Talung (Late Permian) and Daye (Early Triassic) formations at Potuo (POT66T, POT67T, and POT68T) and Laxian (LAX8T, LAX9T, LAX10T, LAX11T, LAX 13T, and LAX14T) were processed for U-Pb zircon dating. Of these, seven ash layers yielded sufficient zircon crystals for CA ID-TIMS U-Pb analyses. Zircon U-Pb isotopic compositions were determined by chemical abrasion, isotope dilution, and thermal ionization mass spectrometry (CA-ID-TIMS) at the University of Geneva, Switzerland, following the procedure described by Widmann et al. (2019). Zircons were extracted from ash beds by conventional methods (crushing, milling, sieving, magnetic and density separation), including hand-picking of high aspect ratio grains free of visible inclusions. The zircon grains were thermally treated at 900°C for 48 hr to stimulate self-annealing prior to partial dissolution in concentrated hydrofluoric acid (HF_{conc}) to remove structurally damaged domains that may have suffered lead (Pb) loss (see Widmann et al. (2019) for the detailed procedure). The partially dissolved grains were then extracted and washed in 6N HCl in 3 ml Savillex beakers overnight (min. 12 h) at 80°C. Further cleaning steps involve cycling of 7N HNO₃ and ultra-sonic bathing prior to loading into 200 µl capsules for dissolution in 2–3 drops of HF_{conc} for 48 hr at 210°C in pressurized Parr™ vessels. A ²⁰²Pb-²⁰⁵Pb-²³³U-²³⁵U tracer solution: ET2535 (EARTHTIME 2535, Condon et al., 2015) was added prior to dissolution, and Pb and U were isolated using ion exchange resin chromatography. Uranium and Pb isotopic compositions were measured on IsotopX Phoenix TIMS at the University of Geneva. Pb was measured using a dynamic peak jumping routine on a Daly ion counting system, while uranium was measured as UO₂ in static mode using 10¹² Ω resistor Faraday amplifiers for samples POT66T, POT67T, POT68T, and using ATONA Faraday amplifiers (with a 30 s integration time) for samples LAX8T and LAX10T. The measured isotopic ratios were corrected for interferences of ²³⁸U¹⁸O¹⁶O on ²³⁵U¹⁶O₂ using ¹⁸O/¹⁶O composition of 0.00205 based on repeat measurements of the U500 standard. Mass fractionation of U was corrected using a double isotope tracer with a ²³⁵U/²³³U of 0.99506 ± 0.005. The Pb blank isotopic compositions are ²⁰⁶Pb/²⁰⁴Pb = 17.43 ± 0.71 (1σ), ²⁰⁷Pb/²⁰⁴Pb = 14.73 ± 0.38 (1σ) and ²⁰⁸Pb/²⁰⁴Pb = 35.58 ± 1.04 (1σ), based on total procedural blank measurements.

U-Pb dates of zircons were calculated using data reduction software Tripoli and ETRedux (Bowring et al., 2011; McLean et al., 2011), and all uncertainties are reported at the 95% confidence interval. The interpreted weighted mean age is reported in the format: “weighted mean” ±X/Y/Z, where X corresponds to analytical uncertainty, Y to analytical + tracer uncertainty and Z to analytical, tracer and decay constant uncertainty (Schoene et al., 2006). All zircon ²⁰⁶Pb/²³⁸U dates were corrected for ²³⁰Th-²³⁸U disequilibrium using a Th/U_{magma} of 3.5 ± 1.0. We discuss dates at the precision level of analytical uncertainty (X), since most U-Pb data in the relevant literature were obtained using the same isotope tracer (ET2535) and mode of analysis (ID-TIMS), effectively eliminating inter-lab uncertainty. Repeat analyses of the ET100 solution (²⁰⁶Pb/²³⁸U age: 100.173 ± 0.003 Ma; Schaltegger et al., 2021) yielded a value of 100.1678 ± 0.0046 Ma (mean square weighted deviation, MSWD = 3.2, $n = 32/40$). One batch comprising 8 ET100 samples was rejected due to anomalous young average age (this batch is internally consistent). Similarly, young, anomalous ET100 ages observed in Schaltegger et al. (2021) were explained

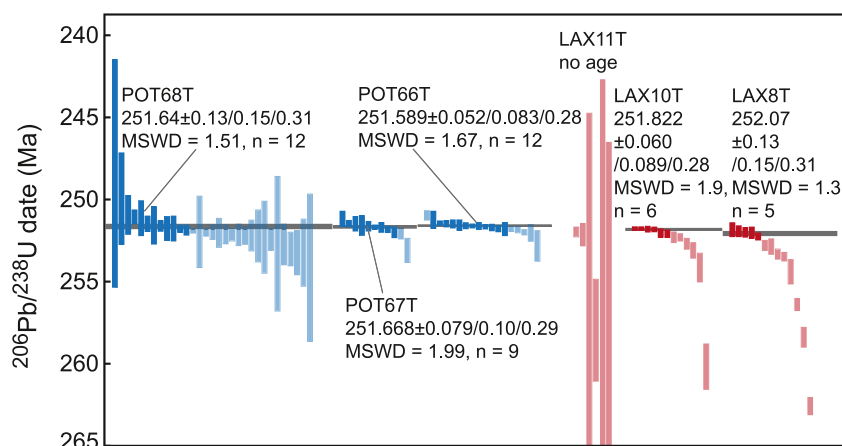


Figure 2. Single-grain zircon analyses and $^{206}\text{Pb}/^{238}\text{U}$ weighted mean dates for volcanic ash beds from Potuo and Laxian. Bars represent single grain zircon U-Pb dates and their uncertainty. Transparent bars are rejected for interpretation (Pb-loss, inheritance, antecrystic).

by fractionation effects during the sample preparation process. Inclusion of this rejected batch would result in an average ET100 age of 100.1639 ± 0.0039 Ma (MSWD = 3.8, $n = 39/40$). Excess scatter is indicated by the elevated MSWD value and is commonly observed for the synthetic ET100 solution. This is potentially derived from instrument instability and from the sample preparation process (Schaltegger et al., 2021).

3. Results

Results of all geochemical analyses are given in Supporting Information S1 and presented in Figures 2–5.

3.1. U-Pb Zircon Geochronology

A total of 98 zircons from seven volcanic ash beds were analyzed. Zircon U and Pb data are presented in Supporting Information S1 and interpreted U-Pb dates are illustrated in Figure 2. For each volcanic ash bed, the U-Pb weighted mean date is interpreted on the following basis: (a) not rejecting any analyses that are concordant, (b) the youngest cluster of interpreted concordant zircons consists of ≥ 3 analyses and (c) assuming that all Pb-loss is effectively removed by the chemical abrasion procedure. This data reduction strategy is in line with previous U-Pb ID-TIMS studies concerning volcanic ash beds straddling the PTB and the Early Triassic (e.g., Augland et al., 2019; Baresel, Bucher, Brosse, et al., 2017; Burgess et al., 2014; Widmann et al., 2020), making all of these previous ID-TIMS ages directly comparable.

Only in one sample (POT66T) do we reject one younger, concordant analysis, as it is younger than the statistically significant, slightly older age plateau of 12 analyses (Figure 2). We assume that this deviation is due to unresolved, residual lead loss not mitigated by the chemical abrasion procedure. Analyses that are older than the youngest, statistically valid, date plateau are considered detrital or due to inherited or antecrystic cores. The principal guideline for the youngest weighted mean age determination is a statistically valid MSWD for the chosen age cluster. Applying this strategy, volcanic ash beds LAX8T, LAX10T, POT66T, POT67T, and POT68T have statistically significant $^{206}\text{Pb}/^{238}\text{U}$ weighted mean ages of $252.07 \pm 0.13/0.15/0.31$ Ma (MSWD = 1.3, $n = 5$), $251.822 \pm 0.060/0.089/0.28$ Ma (MSWD = 1.9, $n = 6$), $251.589 \pm 0.052/0.083/0.28$ Ma (MSWD = 1.67, $n = 12$), $251.668 \pm 0.079/0.10/0.29$ Ma (MSWD = 1.99, $n = 9$) and $251.64 \pm 0.13/0.15/0.31$ Ma (MSWD = 1.5, $n = 12$), respectively (Figure 2). Ash beds LAX14T and LAX11T (Table S1 in Supporting Information S1) did not satisfy the data reduction criteria outlined above and are thus not interpreted.

3.2. TOC Contents and Hg Concentrations

TOC content is stratigraphically variable and generally low for Laxian relative to Potuo with a range between <0.1–0.3 and 0.1–2.9 wt.% respectively (Figure 3). TOC generally shows moderate correlation for Laxian ($r^2 = 0.36$) and Potuo ($r^2 = 0.50$) (Figure 4). Only 3 samples for Laxian have TOC content above 0.2 wt.%, a

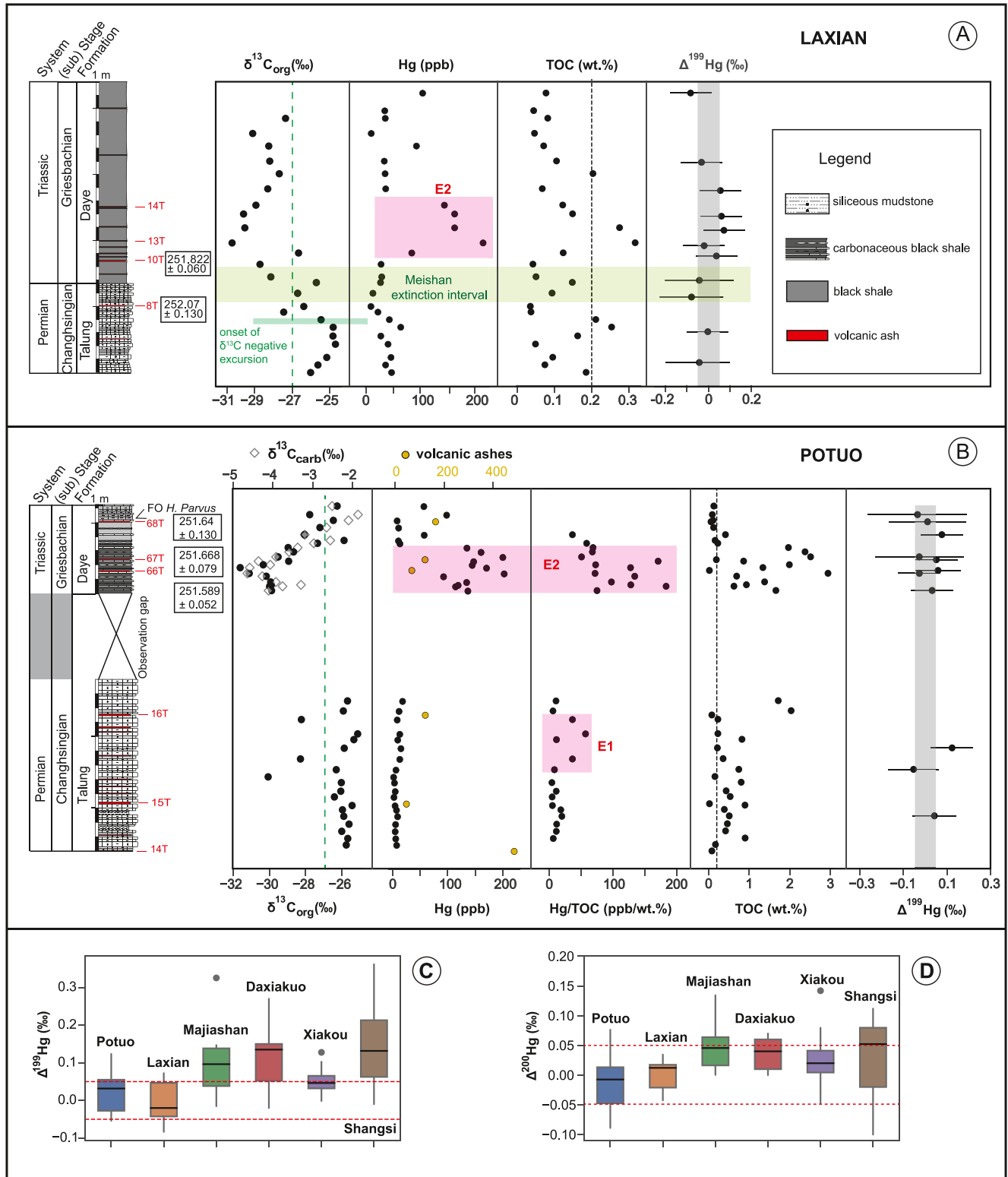


Figure 3.

suggested threshold for robust Hg/TOC normalization (Grasby et al., 2016). In contrast, only 6 out of 38 samples for Potuo have TOC values <0.2 wt.%. Therefore, Hg data for Laxian are not normalized to TOC. OI values for Laxian are high and have a range between 69 and 1,386 mg CO₂/g TOC. OI values are between 3 and 334 mg

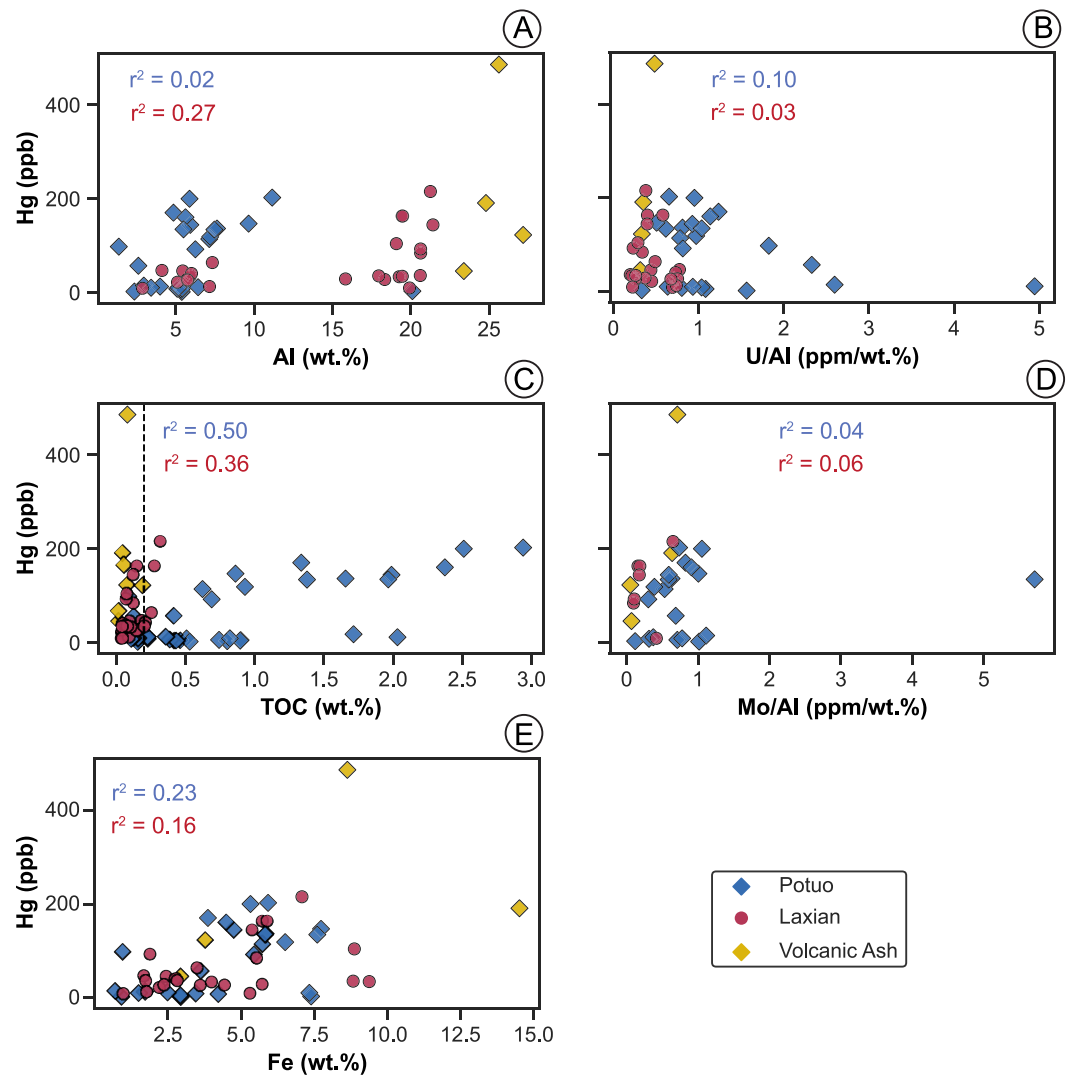


Figure 4. Scatter plot showing the relationship between Hg and (a) Al, (b) U/Al, (c) total organic carbon (TOC), (d) Mo/Al and (e) Fe in the Pingtang syncline sections. Black dashed line represents 0.2 wt.% TOC limit (Grasby et al., 2016). Volcanic ash samples are not included in the calculation of the correlation coefficient squared (r^2).

$\text{CO}_2/\text{g TOC}$ for Potuo, except for volcanic ash samples with values between 64 and 967 mg $\text{CO}_2/\text{g TOC}$. HI values are between 19 and 283 mg HC/g TOC and between 17 and 229 mg HC/g TOC for Potuo and Laxian respectively.

Hg concentrations of samples from the Talung Fm. in Potuo are between 2 and 18 ppb and are generally lower than for Laxian, which have a range between 9 and 64 ppb. The main feature of the latest Permian Hg record for Potuo is a minor Hg/TOC excursion (referred to as E1 here) with a peak Hg/TOC value of 70 ppb/wt.%. In the Daye Fm., a significant Hg concentration increase (here labeled as E2) is recorded in the lower part of the successions at both sections. This Hg excursion is simultaneously expressed by the Hg and Hg/TOC records for Potuo (Figure 3). Peak Hg concentrations within E2 Hg anomaly (Laxian = 251 ppb, Potuo = 203 ppb) are higher than the mean so far reported (62 ppb) for sedimentary rocks (Grasby et al., 2019).

Figure 3. Carbon isotope values, Hg concentrations, Hg/total organic carbon (TOC) ratios, TOC contents and $\Delta^{199}\text{Hg}$ values from (a) Laxian, (b) Potuo. The gap between the Talung and Daye formations in the Potuo stratigraphic log is an observation gap due to coverage by alluvium (Bagherpour et al., 2020). Note that the x-axis for volcanic ash Hg concentrations in (b) is at the top. Black dashed lines represent the 0.2 wt.% TOC limit for Hg/TOC normalization (Grasby et al., 2016) and green dashed lines represent background $\delta^{13}\text{C}_{\text{org}}$ values (-27‰). Box and whisker plots of (c) $\Delta^{199}\text{Hg}$ values and (d) $\Delta^{200}\text{Hg}$ values for Potuo and Laxian compared to those previously documented for other deep-water marine sections in South China. Gray shaded rectangle (in a, b) and red dashed lines (in c, d) represent the interval of no measurable Hg isotope mass independent fractionation (MIF, $0 \pm 0.05\text{‰}$). Data sources are as follows: Majiashan—X. Wang, Cawood, Zhao, Zhao, et al. (2019), Daxiakou—X. D. Wang et al. (2018), Xiakou—J. Shen, Chen, et al. (2019), Shangsi—J. Shen et al. (2021).

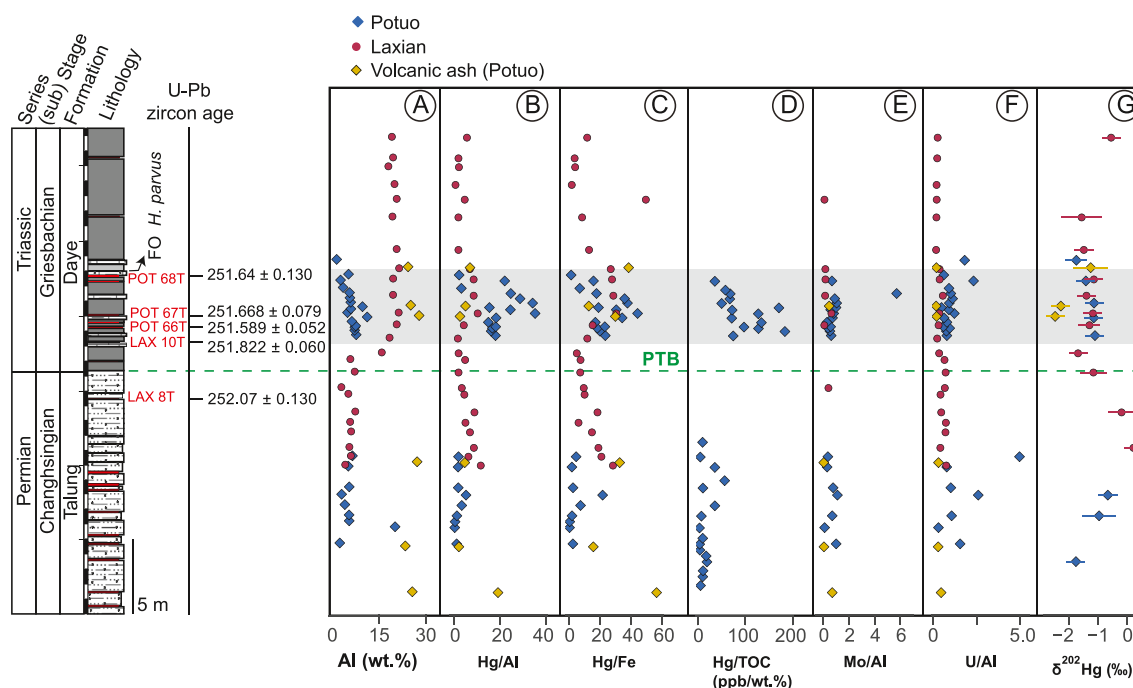


Figure 5. Composite plot of Hg/element ratios and Hg isotope mass-dependent fractionation values for Potuo and Laxian. (a) Al, (b) Hg/Al, (c) Hg/Fe, (d) Hg/total organic carbon, (e) Mo/Al, (f) U/Al, (g) $\delta^{202}\text{Hg}$. Symbols of the lithological log are identical to those of Figure 3. The composite section is based on lithological comparison of the Potuo and Laxian sections (Bagherpour et al., 2020) and assumes similar sedimentation rates for both sections. Note that the Potuo and Laxian sections are only 6.4 km apart and both belong to the Pingtang syncline of the Nanpajiang Basin, recording laterally continuous basinal facies belonging to the Talung Fm. and Daye Fm. (Bagherpour et al., 2020).

Volcanic ashes from the Talung Fm. at Potuo have Hg concentrations that are at least one order of magnitude higher than for interbedded siliceous mudstones. This difference does not hold in the Daye Fm., where Hg concentration values range between 68 and 165 ppb for volcanic ashes and between 84 ppb and 203 for interbedded rocks within the E2 Hg anomaly interval (Figure 3b).

3.3. Mercury Isotopes

Mass-dependent fractionation of Hg isotopes ($\delta^{202}\text{Hg}$) shows near-zero to negative values for both sections throughout the studied interval (range: $+0.23 \pm 0.32\text{‰}$ to $-1.75 \pm 0.32\text{‰}$; mean = $-1.13 \pm 1.02\text{‰}$), except for 2 volcanic ash samples from Potuo with more negative values (Figure 5, POT66T: $-2.49 \pm 0.32\text{‰}$ and POT67T: $-2.29 \pm 0.32\text{‰}$).

Hg isotope MIF ($\Delta^{199}\text{Hg}$ and $\Delta^{200}\text{Hg}$) values for both sections are near-zero throughout the studied interval (i.e., $0.1\text{‰} > z > -0.1\text{‰}$, where z = sample Hg MIF value), except for sample POT 59, which has a $\Delta^{199}\text{Hg}$ value of $0.12 \pm 0.11\text{‰}$. Mean ($\pm 2\sigma$) $\Delta^{199}\text{Hg}$ values are $0.02 \pm 0.11\text{‰}$ and $-0.01 \pm 0.11\text{‰}$ for Potuo and Laxian respectively. For Potuo, the mean $\Delta^{200}\text{Hg}$ value is $-0.01 \pm 0.10\text{‰}$ and for Laxian, it is $0.00 \pm 0.05\text{‰}$. Hence, the Pingtang syncline sections record no measurable MIF of Hg isotopes in contrast to Hg isotope records for deep-water marine sections outside the Nanpanjiang Basin in South China (Figure 3c).

3.4. Major and Trace Elements

Al_2O_3 concentrations for both sections show similar patterns, having lower values in the Talung Fm. (with a range of 2–4 wt.%, except for 1 Potuo sample) relative to the Daye Fm. For Laxian, Al_2O_3 values in the Daye Fm. are 3× higher (range: 15–22 wt.%) than those of the Talung Fm. Fe_2O_3 concentrations show a similar trend to Al_2O_3 , with lower values in the Talung Fm. (1–5 wt.%) relative to the Daye Fm. for both localities. However, unlike Al_2O_3 , values in the Daye Fm. for both localities are identical (between 2 and 9 wt.%). Al and Fe (proxied by Al_2O_3 and Fe_2O_3) show little to no correlation with Hg for both Potuo (Al: $r^2 = 0.02$, Fe: $r^2 = 0.23$) and Laxian

(Al: $r^2 = 0.27$, Fe: $r^2 = 0.16$). Mo and U are redox-sensitive trace elements used to track redox variations in sedimentary environments (Algeo & Maynard, 2004; Hardisty et al., 2018; Tribouillard et al., 2006). Redox-sensitive trace element concentrations are usually normalized to Al to account for variations that may be unrelated to changes in redox conditions, such as changes in sediment input or authigenic mineral formation (e.g., Algeo & Maynard, 2004; Grasby et al., 2013; Rolison et al., 2017). For Laxian, 73% of samples analyzed have Mo contents lower than the lower limit of detection (LLD) of the XRF spectrometer (i.e., 1 ppm). Mo/Al values show no stratigraphic trend for either studied locality (Figure 5e) and have no correlation with Hg contents (Potuo: $r^2 = 0.04$, Laxian: $r^2 = 0.06$; Figure 4d). Laxian samples with measurable Mo ($n = 7$) have Mo/Al values between 0.1 and 0.6 ppm/wt.%. Mo/Al values for Potuo are slightly higher and range between 0.1 and 1.1 ppm/wt.%, except for sample POT 80 with a value of 5.7 ppm/wt.%. Potuo U/Al values range between 0.2 and 2.3 ppm/wt.%, except for sample POT 63 (U/Al = 4.9 ppm/wt.%). For Laxian, U/Al ranges between 0.2 and 0.8 ppm/wt.%. As with Mo/Al, no correlation is observed between Hg and U/Al (Potuo: $r^2 = 0.10$, Laxian: $r^2 = 0.03$; Figure 4b).

Volcanic ash samples have high LOI (loss on ignition) values between 9 and 14 wt.%, consistent with results from contemporaneous ash layers in South China (He et al., 2014). The ash samples have LOI-corrected mean ($\pm 1\sigma$) concentrations of 58 ± 5 , 25 ± 2 , and 5 ± 3 wt.% for SiO_2 , Al_2O_3 and total alkali ($\text{Na}_2\text{O} + \text{K}_2\text{O}$) respectively (Table S2 in Supporting Information S1). To mitigate the chemical effects of secondary alteration of the volcanic ashes, only immobile elements (such as Th, Nb, Ta, Zr, Hf, Ti, Y), known to be unaffected by post-depositional alteration (Portnyagin et al., 2020), are utilized for subsequent chemical classification and tectonic interpretation (Figure 6). The ashes mainly plot within the fields of rhyodacite/dacite, andesite and trachyandesite on the Nb/Y versus Zr/Ti diagram (Winchester & Floyd, 1977), separate from STLIP volcanic rocks, except for 1 sample: POT 14T (Figure 6a). Incompatible trace elements normalized against primitive mantle values (S.-S. Sun & McDonough, 1989) show that the volcanic ashes are characterized by pronounced negative Nb, Ta and Ti anomalies (Figure 6d), similar to the trace element pattern for volcanic ashes from other localities in South China (He et al., 2014; Yang et al., 2012).

4. Discussion

4.1. Sedimentary Hosts of Hg and Interpretation of the Hg Anomalies

4.1.1. Hosts of Hg

Hg enrichment in sediments may reflect enhanced Hg sequestration related to increased abundance of its sedimentary host phase(s) or enhanced Hg input fluxes during sediment deposition (Grasby et al., 2019; J. Shen et al., 2020). Due to the high affinity of Hg for OM, Hg concentration is usually normalized to TOC content to account for any OM increases that could have preferentially enhanced Hg sequestration in sediments (e.g., Grasby et al., 2017, 2019; Sanei et al., 2012). However, in samples with low OM content (<0.2 wt.% TOC), the Hg/TOC ratio is deemed unreliable as the Hg/TOC values become exaggerated, potentially producing false Hg/TOC peaks (Grasby et al., 2016, 2019; but see Yager et al., 2021). In addition to TOC variations, Hg sequestration in sedimentary rocks can be influenced by other sedimentary host phases such as clay minerals, iron oxides and sulfides (Charbonnier et al., 2017; J. Shen et al., 2020).

Based on cross plots of Hg versus TOC, Al, Fe, Mo/Al, and U/Al values for both sections, Hg is best correlated to TOC (r^2 : Potuo = 0.50 and Laxian = 0.36, Figure 4c). This correlation suggests that Hg sequestration in the studied sites was partially controlled by OM availability and may explain the more efficient sequestration of Hg in the black shales of the Daye Formation relative to the siliceous mudstones of the Talung Formation. Nevertheless, plots of Hg/Al and Hg/Fe ratios for both localities, including Hg/TOC for Potuo (Figures 3 and 5) show similar trends of peak Hg contents in the lower part of the Griesbachian record, suggesting that the Hg anomaly in this interval cannot be explained by TOC variability or clay mineral inputs alone. Furthermore, lithological changes are unlikely to control the Hg concentration spike as increases in Hg concentration do not coincide with the change in lithology in either of the two sections. Moreover, relatively high, and low Hg concentrations alike are measured for the Talung and Daye formations where Hg and Hg/TOC anomalies are recorded (Figures 3 and 8).

4.1.2. Evaluation of Hg Preservation

As OM is the dominant host of Hg in the studied successions, the potential impact of post-depositional OM degradation on the Hg record warrants evaluation. Rock-Eval TOC data cross plots (HI , OI , T_{max}) (Figure 7) are

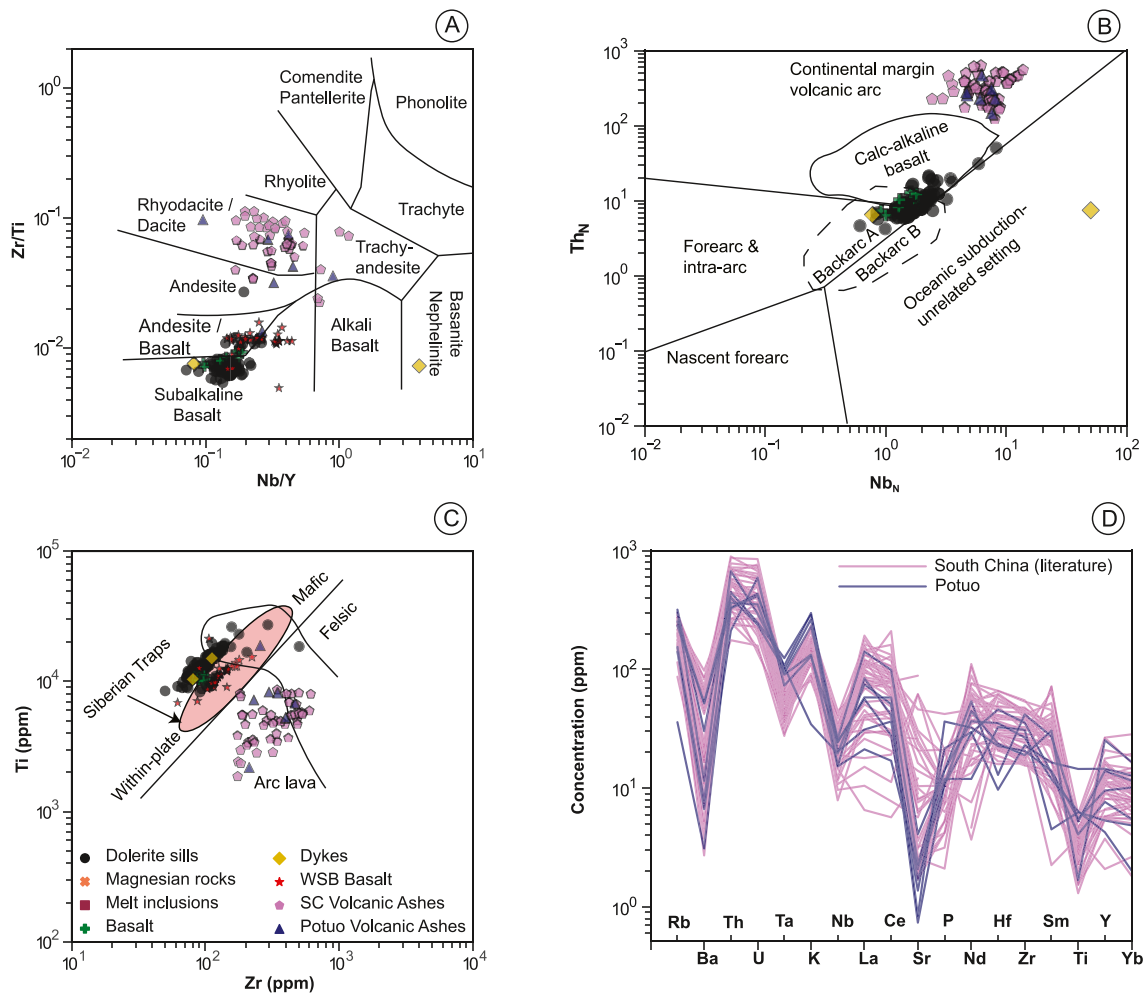


Figure 6. Major and trace element geochemistry results for volcanic ash samples from the Pingtang syncline. (a) Zr/Ti versus Nb/Y classification diagram (Winchester & Floyd, 1977) for volcanic ashes from South China plotted along with volcanic rocks from the Siberian Traps Large Igneous Province (STLIP) (b) N-MORB-normalized Th versus Nb discriminant plot, with tectonic setting interpretation after Saccani et al. (2015, 2018) for volcanic ashes from South China, together with data from dolerite sills, dykes and basalts from the STLIP (Tunguska Basin) plotted for comparison. N-MORB: normal-type mid-oceanic ridge basalt. (c) Ti versus Zr classification diagram after Pearce (1982). The field illustrating typical Siberian Traps volcanic rock compositions is after He et al. (2014). (d) Primitive mantle-normalized spider diagram for Changhsingian and Griesbachian volcanic ashes from Potuo and other localities (Meishan, Chaotian, Jiashi, Rencunping, Shangsi, and Dongpan) in South China. Data for South China localities other than Potuo are from He et al. (2014), Q. Song et al. (2022) and X. Wang, Cawood, Zhao, Chen, et al. (2019). Normalization values for normal-type mid-oceanic ridge basalt and primitive mantle are from S.-S. Sun and McDonough (1989). Data for volcanic rocks from the STLIP are from several sources as follows: basalt flows, dolerite sills, dykes: Sibik et al. (2015), Callegaro et al. (2021), magnesian rocks, melt inclusions: Sobolev et al. (2009); WSB basalts: Reichow et al. (2005). WSB, West Siberia Basin; SC, South China.

routinely used to evaluate the type and maturity of preserved OM in sedimentary successions (e.g., Charbonnier et al., 2020; Espitalié et al., 1985; Fantasia et al., 2018). The low HI and OI values of many of the samples with enough OM for Rock-Eval data interpretation (i.e., TOC > 0.2 wt.%, Figure 7a) may indicate diagenetic alteration of marine OM (altered type II) and/or high input of terrestrial OM (type III) (Charbonnier et al., 2020; Fantasia et al., 2018). The range of T_{max} values (400°C–525°C) suggests that some of the OM in the studied successions are thermally mature and have undergone post-depositional oxidation (Figure 7b; Espitalié et al., 1985). The thermal maturity of preserved OM in some strata of the studied successions suggests that original Hg contents may have been diagenetically modified due to OM loss (Charbonnier et al., 2020). Consequently, the Hg content measured for strata characterized by thermally mature OM may be a minimum estimate of the original Hg content of these rocks.

Despite the probable partial loss of the original Hg content for some samples, several points argue in favor of the reliability of the general Hg trend documented in the present study. The global negative $\delta^{13}C$ excursion

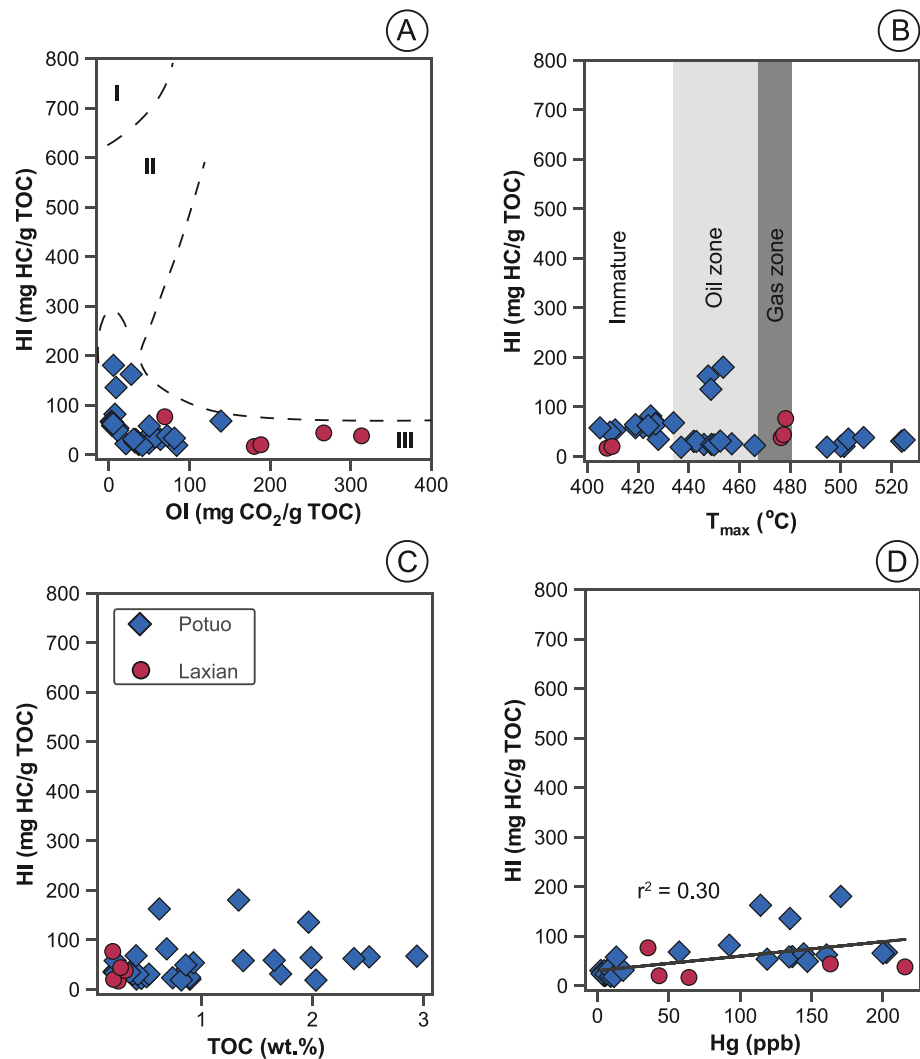


Figure 7. Cross plots of Rock-Eval total organic carbon (TOC) data for samples with TOC >0.2 wt.% to assess the type and quality of preserved organic matter in Potuo and Laxian (modified after Charbonnier et al., 2020). (a) hydrogen index (HI) versus. Oxygen index, (b) HI versus. T_{max} , (c) HI versus. TOC, (d) Hg versus. Hg.

characteristic of the PTB is recorded in both successions, and for Potuo is recorded both for organic and carbonate carbon, similar to the Meishan GSSP (Figure 9). The Changhsingian to Griesbachian Hg trend for both localities is similar despite the vast difference in OM content (Figure 3). The lack (or loss) of OM is more prevalent in the Laxian succession, yet the background Hg content in this succession is 3× that of Potuo. Also, volcanic ashes mostly have similar Hg content in the Talung and Daye Fm. In contrast, interbedded rocks differ strongly in Hg content between these rock formations (Figure 3). The much higher Hg content of volcanic ashes despite their higher susceptibility to weathering (e.g., Jiao et al., 2022) and as such, Hg loss, suggests that (a) Hg is reasonably well preserved in these strata, and (b) the disparity in Hg content between volcanic ashes and interbedded rocks is primary.

Furthermore, both sections record the E2 Hg anomaly, and with similar excursion magnitude (Figures 3 and 8). Similar Hg trends are documented for coeval strata within the Nanpanjiang Basin that is, Kejiao and Xinmin (J. Shen, Chen, et al., 2019). Specifically, the Hg anomaly associated with the PTB in these Nanpanjiang Basin sections is recorded in Griesbachian strata (Figure 9; see also Figures 2, S6, and S7 of J. Shen, Chen, et al., 2019). This similarity between the Changhsingian to Griesbachian Hg trends and hence their spatial reproducibility across the Nanpanjiang Basin indicates that primary Hg concentration trends are preserved in Potuo and Laxian. In addition, there is no correlation between HI and TOC (Figure 7c) and little correlation ($r^2 = 0.30$) between HI

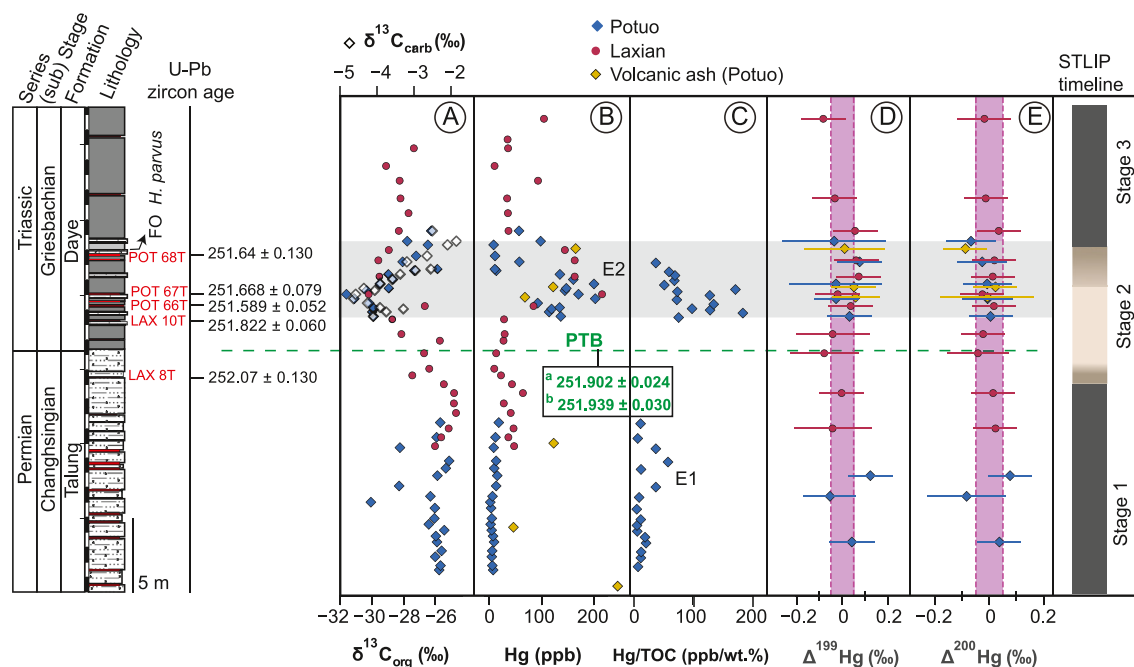


Figure 8. Composite profiles for (a) $\delta^{13}\text{C}$, (b) Hg concentration, (c) Hg/total organic carbon ratios, (d) $\Delta^{199}\text{Hg}$, (e) $\Delta^{200}\text{Hg}$ records from the Potuo and Laxian sections. $\delta^{13}\text{C}$ values are from Bagherpour et al. (2020). The horizontal gray band marks the interval of the Hg concentration spike (E2) and nadir of the negative $\delta^{13}\text{C}$ excursion, and the vertical pink bands depict near-zero Hg isotope mass-independent fractionation ($0 \pm 0.05\text{‰}$, Thibodeau et al., 2016). The dashed green line represents the Talung-Daye formational boundary and the Permian-Triassic boundary (PTB). The Siberian Traps magmatism timeline is after Burgess et al. (2017) and the color gradient between the stages depicts the uncertainty in the timing of the transition between different stages. The PTB on the composite log is defined from the Laxian section as this interval at Potuo is covered by recent alluvial deposits (Bagherpour et al., 2020). U-Pb zircon ages for the PTB (in green) are from (a) Burgess et al. (2014) and (b) Baresel, Bucher, Brosse, et al. (2017). FO, first occurrence.

and Hg values (Figure 7d), suggesting that OM maturity does not influence Hg trends to any large degree in these successions. Also, the E2 Hg anomaly coincides with the climax of the negative $\delta^{13}\text{C}$ excursion at the P-T transition (Figures 3 and 8), suggesting that the Hg trend is controlled by environmental perturbations (as indicated by the $\delta^{13}\text{C}$ excursion), and not by diagenetic alteration. Finally, Charbonnier et al. (2020) noted that despite the oxidative weathering of OM observed for weathered rock samples, there were no significant changes in Hg/TOC ratios, suggesting that the Hg/TOC ratio is less susceptible to the effects of post-depositional OM degradation. In the present study, both Hg anomalies reported are present in the Hg/TOC record and more significantly, the main excursion (E2) is present in both the Hg and Hg/TOC record, suggesting that these Hg trends are primary.

4.1.3. Hg Isotopes

Hg isotopes are used to trace the source(s) and depositional pathway(s) of Hg to natural environments, as Hg isotope MDF ($\delta^{202}\text{Hg}$) and MIF ($\Delta^{199}\text{Hg}$ and $\Delta^{200}\text{Hg}$) compositions vary across Earth surface reservoirs and transport mechanisms (Bergquist & Blum, 2007; Blum et al., 2014; Fu et al., 2021). Here, we focus on Hg isotope MIF, as this occurs via fewer processes compared to MDF (Blum et al., 2014). Also, $\delta^{202}\text{Hg}$ values of direct volcanic emissions overlap with those of terrestrial runoff and atmospheric Hg^{II} deposition (Yager et al., 2021), making them less diagnostic than Hg isotope MIF values.

Hg isotope MIF values are considered to be resistant to diagenetic alteration (e.g., Grasby et al., 2017; Thibodeau et al., 2016). This view was recently strengthened by the experimental study of D. Chen et al. (2022), who documented that high-temperature or high-pressure alteration of rocks does not result in the alteration of $\Delta^{199}\text{Hg}$ and $\Delta^{200}\text{Hg}$ values. $\Delta^{199}\text{Hg}$ is commonly used to interpret the sources and pathways of Hg deposition (Thibodeau & Bergquist, 2017; Yager et al., 2021) and recently, $\Delta^{200}\text{Hg}$ has been proposed as a complementary tracer of Hg sources to land and oceans (Jiskra et al., 2021). This proposition is because even number-Hg isotope MIF (e.g., $\Delta^{200}\text{Hg}$) only occurs via upper atmospheric oxidation-reduction pathways and thus, Hg transformations near Earth's surface yield no measurable even number-Hg isotope MIF (J. Chen et al., 2012; Fu et al., 2021). Hg from terrestrial biomass usually has negative $\Delta^{199}\text{Hg}$ values while oceanic reservoirs (e.g., marine sediments

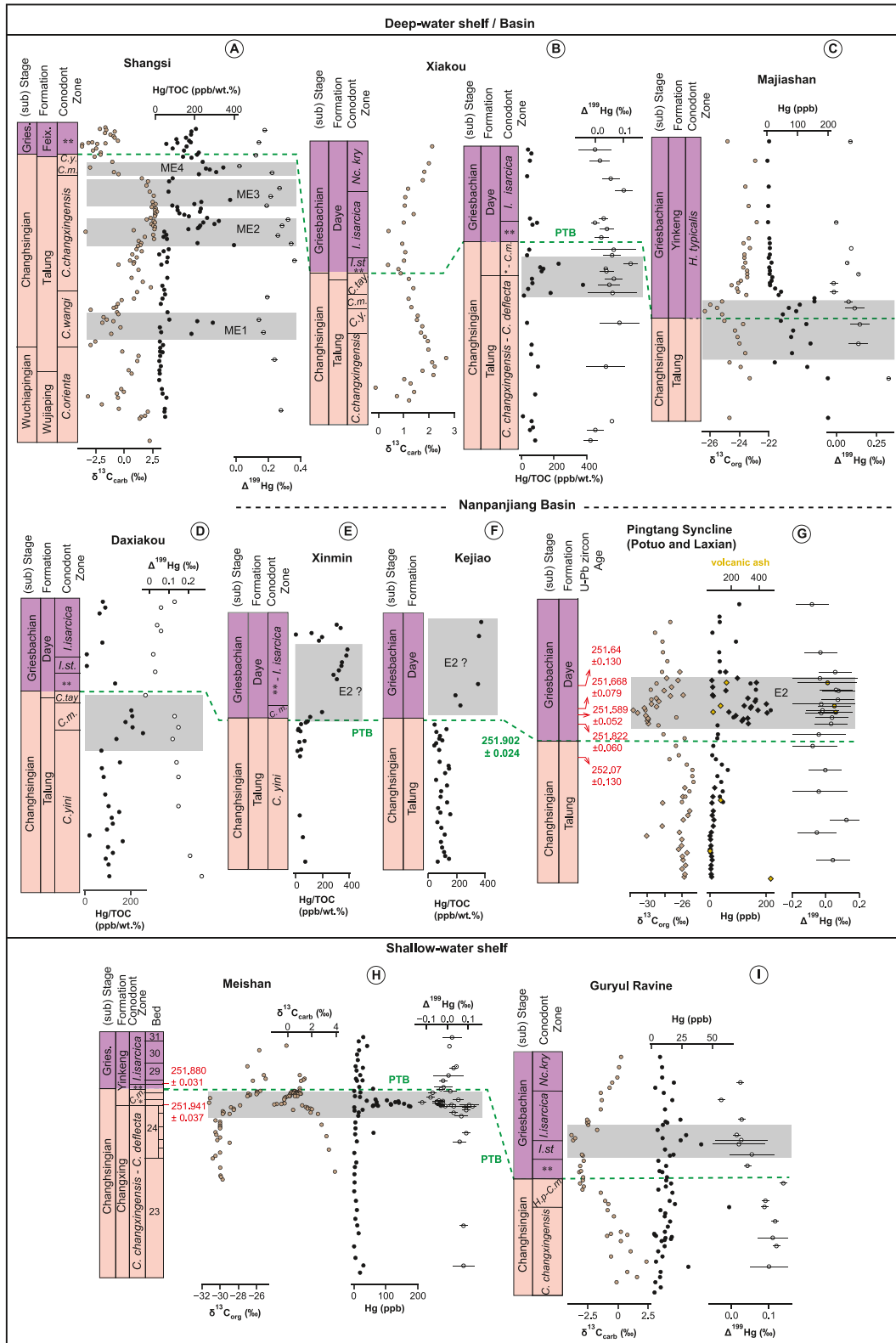


Figure 9.

and seawater) are characterized by near-zero to positive $\Delta^{199}\text{Hg}$ values (Blum et al., 2014; R. Yin et al., 2022). Furthermore, Hg released into the atmosphere may undergo MIF via photochemical reactions during its cycling, acquiring positive or negative MIF values (Blum et al., 2014) before long-term burial in marine sediments (Thibodeau et al., 2016). Hg derived from direct volcanic emission is thought to have no measurable MIF (i.e., $\Delta^{199}\text{Hg}$, $\Delta^{200}\text{Hg} = \sim 0\%$, Thibodeau & Bergquist, 2017; Zambardi et al., 2009), consistent with a recent estimate of the $\Delta^{199}\text{Hg}$ value of the primitive mantle ($0.00 \pm 0.10\%$, Moynier et al., 2021). Therefore, near-zero $\Delta^{199}\text{Hg}$ values recorded for rock samples in the geologic record have been interpreted as reflecting unaltered volcanic Hg input to the depositional environment (e.g., Font et al., 2021; Thibodeau et al., 2016; Yager et al., 2021; H. Zhang, Zhang, & Shen, 2021). Alternatively, near-zero $\Delta^{199}\text{Hg}$ values have also been interpreted as reflecting Hg contributions from a combination of terrestrial and oceanic Hg reservoirs (e.g., J. Shen, Chen, et al., 2019; J. Shen et al., 2021; X. Wang, Cawood, Zhao, Zhao, et al., 2019).

The near-zero and invariant $\Delta^{199}\text{Hg}$ and $\Delta^{200}\text{Hg}$ values throughout our studied interval (Figure 8) are consistent with direct volcanic Hg input from a volcanic center close to the Nanpanjiang Basin, or a mixture of terrestrial and atmospheric/volcanic Hg sources. Several lines of evidence, however, argue in favor of a dominantly atmospheric volcanic Hg source to the studied successions. First, the lack of correlation between Hg and Al suggests that Hg sequestration was unrelated to terrestrial input to the Pingtang syncline. As terrestrial input is characterized by negative Hg isotope MIF values (Thibodeau & Bergquist, 2017; Yager et al., 2021; R. Yin et al., 2022), enhanced clastic input during the Griesbachian (as evidenced by dominantly shale lithology and increase in Al content, Figure 5) is expected to have resulted in more negative $\Delta^{199}\text{Hg}$ values. However, $\Delta^{199}\text{Hg}$ values immediately after the PTB are near-zero to slightly positive for both sites (Figure 3), suggesting that atmospheric volcanic Hg input was the dominant source of Hg to the Nanpanjiang Basin even with potentially higher terrestrial Hg delivery to the basin during the Griesbachian. Second, the Nanpanjiang Basin was situated close to a volcanic center during the P-T transition. This proximity is evidenced by the occurrence of thicker volcanic ash beds in coeval marine successions in southwest South China (i.e., in the Nanpanjiang Basin) relative to the rest of South China (He et al., 2014; T. Y. Zhao et al., 2019), the occurrence of coeval acidic-intermediate volcanic and intrusive rocks in southwestern South China and northern Vietnam, as well as copper concentration and isotope excursions linked to felsic “super-eruptions” in South China during the Changhsingian (H. Zhang, Zhang, Chen, et al., 2021 and references therein). The paleo-location of the Nanpanjiang Basin may, therefore, also explain the disparity between the Pingtang syncline Hg MIF record and those previously published for other parts of South China (e.g., J. Shen et al., 2021; X. Wang, Cawood, Zhao, Zhao, et al., 2019; Figure 3c) (discussed in Section 4.4). Third, the Hg isotope MIF values for volcanic ash samples are indistinguishable from those of overlying and underlying strata, suggesting that the source of Hg for volcanic ashes (TOC = ~ 0) and interbedded rocks (TOC = 0–3 wt.%) were the same. Consequently, the Hg and Hg/TOC anomalies recorded for both localities are interpreted as dominantly reflective of pulses of elevated atmospheric volcanic Hg input to these deep-water marine depositional sites.

4.2. U-Pb Zircon Age Constraints on the Hg Anomaly and C Isotope Excursion

Although previous works (Grasby et al., 2017; J. Shen, Chen, et al., 2019; Sial et al., 2020) indicated a coeval global occurrence of Hg anomalies around the PTBME, the majority of sections with defined Hg anomalies around the P-T transition lack high-resolution, high-precision geochronology. Our study attempts to specifically bracket the age of a well-defined Hg anomaly in the Early Triassic via dating of under and overlying ash beds in expanded deep-water marine records. The new U-Pb zircon ages from the Pingtang syncline span the onset of the latest Permian negative $\delta^{13}\text{C}$ excursion, ca. 252.07 ± 0.130 Ma and brackets a Griesbachian Hg anomaly. The two ash layers analyzed from Laxian straddle the PTB and the U-Pb ages are consistent with the stratigraphy,

Figure 9. Compilation of carbon (organic and carbonate) isotope, mercury (Hg) concentration, Hg/total organic carbon (TOC) and Hg isotope ($\Delta^{199}\text{Hg}$) records for marine depositional environments in the Tethys region: South China and northern India. Hg/TOC ratios are shown only for localities and stratigraphic intervals where TOC content is >0.2 wt.%. (a) Shangsì, (b) Xiakou, (c) Majiashan, (d) Daxiakou, (e) Xinmin, (f) Kejiao, (g) Pingtang syncline (composite of the Potuo and Laxian sections), (h) Meishan. U-Pb zircon ages are from Burgess et al. (2014), (i) Guryul Ravine, northern India. The different profiles are correlated using the Permian-Triassic boundary (PTB) as placed by the authors of the original data sources. Data sources are as follows: Meishan: Cao et al. (2002), Grasby et al. (2017), and J. Shen, Chen, et al. (2019), Guryul Ravine and Majiashan: X. Wang, Cawood, Zhao, Zhao, et al. (2019), Shangsì: J. Shen et al. (2021), Xiakou: J. Shen, Chen, et al. (2019), G. J. Zhang, Zhang, and Shen (2021), Xinmin, Kejiao: J. Shen, Chen, et al. (2019), Daxiakou: X. D. Wang et al. (2018), Pingtang syncline (Potuo, Laxian): this study. U-Pb zircon age for the PTB (in green) is from Burgess et al. (2014). Abbreviations: Gries.: Griesbachian; *: *Hindeodus latidentatus*; C.m.: *Clarkina meishanensis*; **: *Hindeodus parvus*; H.p.: *Hindeodus praeparvus*; I.st.: *Isarcicella staeschei*; Nc.kry.: *Neoclarkina krystyni*; C.y.: *Clarkina yini*; C.tay.: *Clarkina taylorae*.

yielding U-Pb weighted mean ages of 252.07 ± 0.13 Ma (LAX8T, latest Permian) and 251.822 ± 0.060 Ma (LAX10T, Griesbachian) respectively. These U-Pb zircon ages overlap, within analytical error, with the ages of Bed 25 (251.941 ± 0.037 Ma) and Bed 28 (251.880 ± 0.031 Ma) of the very condensed Meishan GSSP (Burgess et al., 2014). Thus, the interval between LAX8T and LAX10T includes the PTBME interval at Meishan and agrees with previous suggestions that the conformable lithological boundary between the Talung/Dalong and Daye/Ziyun formations accurately delineates the PTB in deep-water marine successions in the Nanpanjiang Basin (Bagherpour et al., 2020; Baresel, Bucher, Brosse, et al., 2017). Based on lithological comparisons between Potuo and Laxian, the E1 anomaly in Potuo is stratigraphically below LAX8T (Bagherpour et al., 2020) and as such, likely predates the mass extinction interval. However, the lack of U-Pb ages in the strata spanning E1 makes quantitative comparisons to LAX8T uncertain.

The overlap between the $^{206}\text{Pb}/^{238}\text{U}$ weighted mean ages of ash beds POT66T, 67T, and 68T suggests the occurrence of several successive volcanic eruptions (within the time covered by these volcanic ash layers) at intervals shorter than the resolving power of our ID-TIMS U-Pb geochronology at the given quality of zircon available for this study. Nevertheless, as these volcanic ash layers from Potuo straddle both the Hg anomaly recorded in the Daye Fm., as well as the coeval nadir of the negative $\delta^{13}\text{C}$ excursion (Figure 8), the age of both the Hg anomaly (E2) and peak C-cycle perturbation during the P-T transition can be determined. The youngest age for both the peak of the E2 Hg anomaly and the nadir of the $\delta^{13}\text{C}$ excursion is 251.589 ± 0.052 Ma (POT66T, Figure 8), while the oldest age estimate is 251.668 ± 0.079 Ma (POT67T). These two ages are identical within the analytical (X) uncertainty, precluding an estimation of the duration of the Hg anomaly. Despite these uncertainties, we can establish with confidence that the post-PTB Hg anomaly peak observed in Potuo is ca. 300 kyr younger (largely outside of analytical uncertainty) than the Meishan PTBME interval (Burgess & Bowring, 2015; Burgess et al., 2014), as well as the extinction horizon in Penglaitan (251.939 ± 0.031 Ma; S. Z. Shen, Ramezani, et al., 2019).

4.2.1. Hg Anomalies as a PTBME Correlation Tool

A negative $\delta^{13}\text{C}$ excursion at the P-T transition together with a Hg anomaly are common features of many PTB-straddling sedimentary successions (Figure 9). As such, the peak of the Hg anomaly and/or the nadir of the negative $\delta^{13}\text{C}$ excursion associated with the PTB are often considered to be stratigraphic markers for the PTB extinction interval (e.g., Grasby et al., 2017; Sial et al., 2020; J. Shen, Chen, et al., 2019; J. Shen et al., 2023; Wignall et al., 1998). Although some sedimentary successions, especially in high latitudes, show Hg excursions coincident with both the negative $\delta^{13}\text{C}$ excursion and mass extinction (e.g., Grasby et al., 2013; Sanei et al., 2012), it is apparent that Hg excursions in several other successions straddling the PTB vary in expression, timing, and vertical stratigraphic extent (Figure 9). Furthermore, local post-depositional processes (e.g., weathering and burial diagenesis) may lead to the loss of Hg sequestered in rocks, altering the Hg record of these successions (Charbonnier et al., 2020). As such, Hg loss due to post-depositional alteration may partly explain the locally variable expression of Hg anomalies observed for many PTB successions (Figure 9). However, a thorough assessment of the degree of preservation of rock successions from which P-T transition Hg records have been published would be required to fully explore this possibility. Therefore, the variability of PTB Hg records across different localities questions the reliability of these Hg anomalies for positioning the PTBME, as well as the use of Hg anomalies as a stratigraphic correlation tool in general.

In the case of the Pingtang syncline record, neither Hg excursion (E1 nor E2) temporally corresponds to the extinction interval as calibrated in the Meishan GSSP (Figures 3 and 8). Also, no Hg anomaly is recorded at the PTBME extinction interval in Laxian (i.e., between LAX 8T and 10T, Figure 3), although the equivalent stratigraphical interval in Potuo is a visibility gap (Bagherpour et al., 2020). As such, the presence of a Hg anomaly there cannot be formally excluded. Nevertheless, our U-Pb zircon ages show that both the nadir of the PTB-negative $\delta^{13}\text{C}$ excursion and the peak of the stratigraphically nearest Hg anomaly to the PTB (E2) are of Griesbachian age (between 251.589 ± 0.052 and 251.668 ± 0.079 Ma). The peak of these excursions therefore correlates with Bed 33 of the Meishan GSSP (251.583 ± 0.086 Ma, Burgess et al., 2014), which is much younger than the PTB. Thus, these data provide evidence that although Hg anomalies may coincide with the nadir of the PTB-negative $\delta^{13}\text{C}$ excursion (Figure 9), this correspondence cannot be reliably used as a stratigraphic marker for the PTBME in a single section or between different sections (and/or different basins). Similar conclusions were reached for the end-Triassic extinction (ETE) event by Yager et al. (2021), who documented “mismatches in timing” between Triassic-Jurassic boundary Hg anomalies and Central Atlantic Magmatic Province (CAMP)

magmatism, which is purported to have triggered the ETE event. The validity of Hg anomalies as a stratigraphic correlation tool has also been questioned for other intervals of the geologic record, including the Toarcian (Them et al., 2019), Cretaceous-Paleogene (Fendley et al., 2019; Percival et al., 2018) and the Late Devonian (Liu et al., 2021; H. Zhao et al., 2022). Hence, positioning the PTB extinction event by means of and/or correlation based on Hg chemostratigraphy should be treated with extreme caution.

The $\delta^{13}\text{C}$ record from Tethyan marine successions (Figure 9) indicates that the expression of the PTB $\delta^{13}\text{C}$ excursion varies between different sections (as previously alluded to by S. Z. Shen, Ramezani, et al., 2019). Nevertheless, the PTB (as determined for the individual sections), appears to approximately correspond to the midpoint, not the nadir, of the negative $\delta^{13}\text{C}$ excursion in successions not affected by stratigraphic condensation (e.g., Meishan) or a PTB hiatus (Figure 9). Therefore, it is suggested that in the absence of high-resolution U-Pb zircon age calibration, an approximate correlation of the PTB extinction interval could be achieved using the midpoint of the PTB-negative $\delta^{13}\text{C}$ excursion. This correlation strategy could be most effective for sections lacking robust biochronology and where the P-T transition $\delta^{13}\text{C}$ record is not truncated by a hiatus.

4.3. Does the E2 Hg Anomaly of Griesbachian Age Coincide With a Second Extinction Event?

The onset of the Griesbachian Hg anomaly as recorded from the Laxian section (Figure 3) postdates LAX10T, which is dated at 251.822 ± 0.060 Ma. This age coincides, within analytical uncertainty, with that determined for Bed 28 at the Meishan GSSP (251.880 ± 0.031 Ma; Burgess et al., 2014). Because a second step of the PTB mass extinction has been postulated to have occurred within Bed 28 in Meishan (H. Song et al., 2013), it is pertinent to consider whether the E2 Hg anomaly is associated with this proposed second extinction step.

Conodont biozones around the PTB are usually interval zones (IZs), with the base of each IZ being defined by the first occurrence (FO) of an index species and the top defined by the base of the next overlying IZ. However, this biostratigraphical correlation technique often leads to diachronous correlations because the relative stratigraphic order of FOs of index species is not constant across space, as demonstrated by Brosse et al. (2016) for conodonts around the PTB in South China (see also Ellwood et al., 2017). Reasons for diachronous IZs include ecological control over the distribution of species in time and space, sampling effort, selective preservation, and hiatuses in the sedimentary record (Guex, 1991; Holland & Patzkowsky, 2015; Leu et al., 2022). However, following this approach, the “legal” base Triassic was defined by the FO of *Hindeodus parvus* in the very condensed Meishan section (H. Yin et al., 2001).

H. Song et al. (2013) compiled FOs and LOs (last local occurrences) for conodonts and benthic taxa from seven South Chinese PTB sections (including Meishan and Shangsi), which led the authors to propose two extinction steps. The main and older event was placed at the base of the *C. meishanensis* IZ, the antepenultimate IZ below the FO of *H. parvus*. The proposed second extinction step, of lesser magnitude, was found at the base of the *I. isarcica* IZ, which is the third Triassic IZ above the spatially variable FO of *H. parvus*. However, a recent thorough re-investigation of Late Permian conodont IZs in the more expanded Shangsi section (Yuan et al., 2019) led to a revision of the basal Triassic into the *C. meishanensis* IZ. This new placement of the base of the Triassic (Yuan et al., 2019; written comm. 2022) in the *C. meishanensis* IZ in Shangsi and Meishan has the intrinsic benefit of coinciding with both the main extinction event and the lithostratigraphic boundary between Permian and Triassic rock units, which is marked by a hiatus in outer shelves and shallower depositional settings in South China and elsewhere (Bagherpour et al., 2017; H. Yin et al., 2014). Close examination of the raw biostratigraphic data (Table S2 of H. Song et al., 2013) from which a second extinction step was postulated shows no consistent extinction in the relative timing of the different species across the data set. Extinction of a given clade occurs in a single section, or pair of sections at the very best, thus undermining arguments in favor of a second extinction event of global significance. For instance, only the condensed Meishan section displays an apparent second step for benthic foraminifers and bivalves. In Shangsi, no second extinction emerges for any benthic clade around the base of the *I. isarcica* IZ.

Furthermore, the compositing of local extinction patterns (H. Song et al., 2013) relies on the implicit assumption of synchronous conodont IZs. However, as the seven sections of this data set cover a very broad range of water depths, ranging from lagoon-shoals to lower slope-basins (Table S1 of H. Song et al., 2013), the assumption of synchronous conodont IZs becomes untenable. It is also at variance with the fact that the respective bathymetric distribution of segminate and segminiplanate conodonts, both involved as index species of IZs, is known to be

spatially controlled by temperature—that is, depth of water masses (Joachimski et al., 2012; Leu et al., 2019). Moreover, the general development of a hiatus spanning approximately the entire *C. meishanensis* IZ in shallower depositional settings as clearly established by H. Yin et al. (2014) automatically excludes any synchronicity of the neighboring IZ when comparing to hiatus-free deep-water sections.

Consequently, because (a) the presence of a stratigraphic hiatus in some sections will inevitably generate a spurious extinction event and (b) conodont IZs across a depth gradient ranging from lagoonal to basinal depositional settings can hardly be synchronous, there is insufficient biostratigraphic evidence to support a second extinction event in South China. Consequently, it is concluded that the E2 Griesbachian Hg anomaly reported here is not associated with a second extinction pulse in South China.

4.4. Provenance of Volcanic Hg Input

Our U-Pb geochronological results allow us to place the Pingtang syncline Hg record within the temporal framework of STLIP magmatism (Burgess & Bowring, 2015; Burgess et al., 2017), a prominently discussed source of volatiles and toxic elements (such as Hg) during the P-T transition (Black et al., 2012; Broadley et al., 2018; Sibik et al., 2021; H. H. Svensen et al., 2018). A maximum duration for intrusive and extrusive magmatic STLIP activity is given by the bracketing ages of 252.27 ± 0.11 Ma (Burgess & Bowring, 2015) to 250.60 ± 0.22 Ma (Augland et al., 2019), the latter from syenitic intrusions with an uncertain relationship to the STLIP. Therefore, STLIP magmatism, being active during the studied interval, is a potential source of volcanic Hg input to South China during the P-T transition.

However, several studies have demonstrated that more proximal regional volcanic activity related to convergent plate tectonism and subduction magmatism occurred during the P-T transition, which led to elevated Hg concentrations and may have contributed to the PTBME in South China (Gao et al., 2013; He et al., 2014; Jiao et al., 2022; H. Zhang, Zhang, & Shen, 2021; T. Y. Zhao et al., 2019; Zheng et al., 2020). In addition to Hg/TOC anomalies close to the PTBME horizon, Hg/TOC excursions and corresponding Hg isotope compositions have been documented for the earliest Triassic (Griesbachian) from South China and northern India (X. D. Wang et al., 2018; X. Wang, Cawood, Zhao, Zhao, et al., 2019). X. Wang, Cawood, Zhao, Zhao, et al. (2019) documented a pair of Hg/TOC anomalies in the latest Permian and earliest Triassic, respectively, accompanied by a decreasing trend of $\Delta^{199}\text{Hg}$ values from the Changhsingian to the Griesbachian. Based on this $\Delta^{199}\text{Hg}$ trend, they interpreted their Griesbachian Hg/TOC excursion as having resulted from terrestrial Hg input due to elevated Early Triassic continental weathering. Recently, J. Shen et al. (2021) reported several Hg enrichment intervals predating the PTBME (named ME1-ME3), as well as one interval coeval with the PTBME (ME4), from three marine sections in South China. These authors reported the same pattern of decreasing $\Delta^{199}\text{Hg}$ values from the Changhsingian to Griesbachian. The Hg anomalies preceding the PTBME were interpreted to reflect regional subduction-related volcanism due to their spatial restriction to the Tethys region, the occurrence of numerous volcanic ash layers in Upper Permian rocks across South China, and the geochemical composition of zircons in these ash layers supporting a subduction-zone volcanic arc origin.

In contrast with previous studies, the $\Delta^{199}\text{Hg}$ values in the current study remain near-zero throughout the studied interval and are slightly positive within the Griesbachian E2 anomaly (Figure 8). This $\Delta^{199}\text{Hg}$ trend, despite variations in OM content and detrital flux, is consistent with a constant dominant atmospheric volcanic Hg source relatively close to the Nanpanjiang Basin during the studied interval. The disparity between the Hg isotope MIF record of the Pingtang syncline and other deep-water marine records in South China (e.g., X. Wang, Cawood, Zhao, Zhao, et al., 2019; J. Shen et al., 2021) (Figure 9), however, suggests that: (a) Hg sequestered in PTB-straddling marine successions in different parts of South China do not have the same source/depositional pathway, and (b) Hg isotope compositions alone may not be sufficient for discriminating between different potential volcanic sources of Hg (e.g., Siberian Traps volcanism or regional arc volcanism) to deep-water depositional sites during the P-T transition in South China.

Given that (a) Hg excursions in the Pingtang syncline successions are recorded in strata with numerous interbedded volcanic ash layers (which have high Hg content throughout the studied interval, Figure 3), (b) the $\Delta^{199}\text{Hg}$ values of these ashes are indistinguishable from those of interbedded rocks, and (c) the Nanpanjiang Basin was situated close to a volcanic center during the P-T transition, we postulate that the major and trace element geochemical properties of these volcanic ashes can be used to trace the origin of volcanic Hg inputs to these successions. The

analyzed volcanic ash beds from Potuo have major and trace element characteristics similar to previously studied volcanic ashes from South China (Figure 6) (He et al., 2014; X. Wang, Cawood, Zhao, Chen, et al., 2019). Their primitive mantle-normalized trace element compositions (S.-S. Sun & McDonough, 1989) are characterized by depletions in Ta, Nb, Sr, and Ti, similar to rocks from subduction settings (Pearce et al., 1995). The ashes show intermediate to acidic chemical compositions, plotting in the field of basaltic andesite, trachy-andesite and rhyolite/dacite (Figure 6a), and are chemically distinct from volcanic rocks originating from the STLIP (Callegaro et al., 2021; Reichow et al., 2005; Sibik et al., 2015; Sobolev et al., 2009). In addition, a mid-oceanic ridge basalt (MORB)-normalized trace element (Th vs. Nb) discriminant plot (Saccani et al., 2015, 2018) of the volcanic ashes from the Pingtang syncline suggests that they originate from a continental margin volcanic arc tectonic setting (Figure 6b). Similar conclusions were reached for other volcanic ashes from successions straddling the PTB in South China, in that these ashes have no genetic link to the Siberian Traps, but instead derived from subduction zone arc volcanism in the Tethys region (Gao et al., 2013; He et al., 2014; Jiao et al., 2022; Q. Song et al., 2022; T. Y. Zhao et al., 2019).

Consequently, we conclude that episodic regional arc volcanism associated with convergent plate tectonics in the Tethys region best explains the elevated Hg input to the Nanpanjiang Basin as recorded in the Pingtang syncline during Changhsingian to Griesbachian times. Furthermore, based on general atmospheric circulation models, previous studies have suggested that the Canadian Arctic was favorably positioned to receive volatiles (including volcanic ash) from the STLIP during the Permian to Triassic because it was situated downwind relative to the location of the STLIP eruptions (Dal Corso et al., 2022; Grasby et al., 2011, 2013). In this scenario, the South China region, being located toward the southeast and several thousands of kilometers away from Siberia, would have been poorly situated to receive volatiles from the STLIP. Nevertheless, STLIP Hg contributions to South China cannot be ruled out. Finally, as noted by J. Shen et al. (2023), volcanic arc magmatism along the eastern margin of the PaleoTethys was especially active during the Permian to Triassic, as inferred from abundant volcanic ash beds in coeval strata, the distribution of volcanic rocks, as well as a number of associated Hg anomalies across the PTB in this region (Figure 9).

4.5. Hg Anomalies, $\delta^{13}\text{C}$ Excursions and Volcanism During the P-T Transition

Owing to the paucity of U-Pb zircon ages for deep-water sections from which Hg anomalies have been reported in South China, it is difficult to confidently correlate our recorded Hg anomalies with those reported for other localities in the Tethys region. However, the E1 anomaly recorded from the studied successions together with ME2 and ME3 episodes of J. Shen et al. (2021), indicate that Hg anomalies preceding the PTB extinction are recorded in both shallow and deep-marine settings in South China. In contrast, the E2 Griesbachian Hg anomaly is not recorded from any shallow-water marine section nor deep-water sections in South China, except for deep-water sections in the Nanpanjiang Basin (e.g., Xinmin, Kejiao; Figure 9). Nevertheless, E2 may be coeval with the Hg anomaly recorded between the *I. staeschei* and *I. isarica* conodont zones (X. Wang, Cawood, Zhao, Zhao, et al., 2019), which also coincides with the nadir of the PTB-straddling negative $\delta^{13}\text{C}$ excursion in the southwestern Tethys Guryul Ravine section (Figure 9). However, further work from other marine successions with precise U-Pb zircon ages is required to confirm the spatial extent of the Griesbachian Hg anomaly.

The (stratigraphically variable) coincidence of the nadir of $\delta^{13}\text{C}$ excursions with Hg anomalies in the Pingtang syncline and other Tethyan successions (Figure 9) hints at a common driving factor—volcanism. The global distribution of $\delta^{13}\text{C}$ excursions and Hg anomalies close to the PTB in P-T successions (Baud et al., 1996; Grasby et al., 2013; Korte & Kozur, 2010; Sanei et al., 2012; J. Shen, Chen, et al., 2019) argues in favor of a large-scale volcanic degassing episode, such as that of the STLIP, as the ultimate cause of drastic environmental changes of global extent. The onset of the negative $\delta^{13}\text{C}$ excursion in the Pingtang syncline starts just before deposition of the ash layer (LAX8T) at 252.07 ± 0.130 Ma (Figure 8) and is characterized by an initial 2‰ decrease in $\delta^{13}\text{C}$ values in the upper Changhsingian followed by a further 3‰ decrease in the lower Griesbachian. This onset of $\delta^{13}\text{C}$ excursion may temporally overlap with the transition from the extrusive Stage 1 to intrusive Stage 2 of STLIP magmatism, proposed to have occurred at about 251.9 Ma (Burgess et al., 2017). Stage 2 STLIP magmatism was characterized by the intrusion of dykes and sills into country rocks in the Tunguska Basin (Burgess & Bowring, 2015; Burgess et al., 2017). The intrusions, and subsequent sill complex formation, are proposed to have caused the injection of massive amounts of both CO_2 and CH_4 into the atmosphere via contact metamorphism of coal beds, shales and petroleum-bearing evaporites in the Tunguska Basin (Burgess et al., 2017; H.

Svensen et al., 2009; H. H. Svensen et al., 2018), which collectively are thought to result in a >5‰-negative $\delta^{13}\text{C}$ excursion.

However, Davydov (2021) recently questioned the validity of this sill-rock thermal interaction model, pointing out that there is no correlation between coal metamorphism and the distribution of sills in the Tunguska Basin. This author also argued that the role of contact metamorphism by undifferentiated intrusions, which constitute >95% of the Tunguska Basin intrusions, was limited and insignificant to the general coal metamorphism in the Tunguska Basin, and that coal metamorphism in the Tunguska Basin was probably related to regional tectonic deformation instead of magmatism. Furthermore, the role of intrusive STLIP magmatism as a potential driver of the global carbon cycle perturbations and mass extinction during the P-T transition is questioned. This stems from the uncertainty regarding the age of the explosion pipes in the Tunguska Basin (which could have transported CO_2 and other gases such as Hg to the atmosphere), as well as the U-Pb ages of the sill intrusions that violate stratigraphic superposition (Davydov, 2021). Consequently, additional U-Pb zircon geochronologic calibrations of STLIP intrusive rocks are required to resolve these questions.

Pending the resolution of these questions, an additional but not mutually exclusive explanation that could reconcile the coincidence of negative $\delta^{13}\text{C}$ excursions and Hg anomalies recorded at a global scale during the P-T transition can be considered. This is that concurrent regional arc volcanism in different palaeocontinents was responsible for both CO_2 and Hg release resulting in the $\delta^{13}\text{C}$ excursions and Hg anomalies. In addition to South China, extensive regional arc volcanism during the P-T transition has been documented for many spatially disparate localities. Some of these include the northern Patagonian Massif, Argentina (Luppo et al., 2018), Antarctica (Nelson & Cottle, 2019), Australia (Chapman et al., 2022; Metcalfe et al., 2015), and Karoo Basin, South Africa (Gastaldo et al., 2020), with coeval Hg anomalies also recently documented for the latter two (J. Shen et al., 2023). The suggestion of concurrent regional arc volcanism in several paleocontinents during the P-T transition is congruent with recent suggestions of a Pangean “ring of fire” (subduction-related volcanism along the convergent Panthalassan margin of Pangea) as an explanation for marine and terrestrial environmental perturbations during the latest Permian (Vajda et al., 2020).

Reasons for a global increase in regional arc volcanism concurrent with STLIP volcanism are still uncertain. Jiao et al. (2022) recently suggested that the ascent of the STLIP mantle plume may have triggered volcanic activity in several subduction zone systems. While the effect of a large mantle plume on global plate tectonics is highly debatable, STLIP volcanism occurred in a context of global increase of accretion and subduction rates from the Permian to Triassic (Vérard et al., 2015b, their Figure 11a), which has also been linked with Early Triassic sea-level rise (Vérard et al., 2015a, their Figure 17). However, such global increase in subduction rates is likely to occur over tens of millions of years. Hence, increased regional arc volcanism over hundreds of thousands of years between the latest Permian to earliest Triassic may be totally disconnected from global tectonics. Irrespective of the reasons for this global increase in arc volcanism over the P-T transition, our results from the Pingtang syncline suggest that volcanic activity linked to Hg anomalies and C-isotope excursion probably peaked between 251.589 ± 0.052 and 251.668 ± 0.079 Ma in the Nanpanjiang Basin, South China (Figure 8).

4.6. Implications for the PTBME

While it is generally accepted that STLIP magmatism exerted a major control on the global carbon budget and mercury cycle during the Paleozoic to Mesozoic transition, it is clear that South China was substantially influenced by nearby volcanic centers throughout the Late Permian to Triassic (He et al., 2014; H. Zhang, Zhang, & Shen, 2021). This is evident from the older and well-known Emeishan LIP (Huang et al., 2022), the occurrence of P-T volcanic rocks especially in southwest South China (Gao et al., 2013), the abundant volcanic ash layers within P-T marine sedimentary successions, shown to be genetically distinct from STLIP rocks (Gao et al., 2013; He et al., 2014; Yang et al., 2012), as well as Changhsingian Hg/TOC anomalies restricted to the Tethys region (J. Shen et al., 2021; this study). In addition, regional arc volcanism has been linked to notably decreased carbonate and biogenic silica production, as well as decreased water column oxygenation in South China (J. Shen, Cao, et al., 2013). The temporal overlap between regional intermediate to felsic volcanism and the basaltic volcanism from the STLIP thus supports a scenario in which STLIP magmatism and concurrent subduction-related regional arc volcanism in the Tethys region may have acted in concert to generate pernicious environmental conditions for marine and terrestrial faunas in South China during the Late Permian (J. Shen, Cao, et al., 2013; S. Z. Shen, Ramezani, et al., 2019; J. Shen et al., 2021).

The finding of several sudden increases in mercury concentration that both predate and post-date the PTBME event is significant. This is because these Hg enrichments suggest that elevated volcanic activity, which is thought to have triggered the PTBME in South China, was not restricted only to a short interval for example, within Stage 2 STLIP magmatism (Burgess et al., 2017), but rather took place over several thousands of years during the P-T transition. Thus, repeated bursts of regional felsic and intermediate volcanism (and resulting increases in mercury concentration) could have had a cumulative adverse effect on the environment and the species that lived at the time, making them more vulnerable to extinction (J. Shen, Cao, et al., 2013; S. Z. Shen, Ramezani, et al., 2019; J. Shen et al., 2021). Subsequently, significant environmental stresses resulting from STLIP magmatism would have quite easily pushed faunas in South China “over the edge” to bring about the mass extinction at the Paleozoic-Mesozoic transition. This scenario is similar to that proposed by Racki (2020) for the Late Devonian Kellwasser Crisis.

5. Conclusions

The present study establishes the Hg and $\delta^{13}\text{C}$ records of two deep-water marine successions in the Nanpanjiang Basin, South China, spanning the Changhsingian to Griesbachian. U-Pb zircon ages and Hg/TOC ratios indicate elevated volcanic activity before 252.07 ± 0.130 Ma (preceding the PTBME) and during several episodes in the Griesbachian, peaking between 251.589 ± 0.052 and 251.668 ± 0.079 Ma. The latter range in ages is coeval with the nadir of a large negative C isotope excursion, similar in magnitude to the global excursion at the PTB. Based on evidence from the coupled $\delta^{13}\text{C}$ and Hg records, major and trace element geochemistry of volcanic ashes, and the U-Pb zircon age constraints, we conclude that the recorded Hg enrichments are primarily sourced from subduction-related arc volcanism in the Tethys region. Consequently, our Hg record together with recent results from South China documenting several episodes of Hg enrichment during the P-T transition is compatible with previous suggestions that arc volcanism contributed to environmental deterioration and biodiversity decline in South China leading up to the PTBME, which was triggered by STLIP magmatism. Our study provides an absolute timeframe within which Late Permian to Early Triassic Hg and $\delta^{13}\text{C}$ records from different deep-water successions (which are less likely to contain stratigraphic gaps) in South China can be calibrated. This precise, radioisotopic timeframe allows for a more in-depth assessment of the relation between volcanism, environmental changes, and the mass extinction event at the P-T transition.

Conflict of Interest

The authors declare no conflicts of interest relevant to this study.

Data Availability Statement

The data set associated with the current study is available on Zenodo (Edward et al., 2023). Figure 1 was made based on the Panalexis model (Vérard, 2019) using ArcGIS®. Figures 2–8 were made with Matplotlib version 3.5.2 (Caswell et al., 2022), available under the Matplotlib license at <https://matplotlib.org>, and seaborn version 0.11.2 (Waskom, 2021), available at <https://pypi.org/project/seaborn/>. All figures were edited using Adobe Illustrator®.

Acknowledgments

This research was supported by a Swiss National Science Foundation Sinergia Grant (project nr. CRSII5_180253). We thank Olivier Reubi, Edson Ramudzuli and Jérôme Chmeleff for analytical assistance. Special thanks to Borhan Bagherpour and Marc Leu for providing logs for the study sections, and to members of the Sinergia PaleoC4 team for discussions during the development of this manuscript. The authors also thank Kuang Guodong (Geological survey of Guanxi), Ji Cheng (NIGPAS), and Shen Shuzhong (University of Nanjing) for their help related to fieldwork and for scientific discussions. Three anonymous reviewers are also thanked for their comments, which helped improve the manuscript.

References

- Algeo, T. J., & Maynard, J. B. (2004). Trace-element behavior and redox facies in core shales of Upper Pennsylvanian Kansas-type cyclothems. *Chemical Geology*, 206(3–4), 289–318. <https://doi.org/10.1016/j.chemgeo.2003.12.009>
- Augland, L. E., Ryabov, V. V., Vernikovsky, V. A., Planke, S., Polozov, A., Callegaro, S., et al. (2019). The main pulse of the Siberian Traps expanded in size and composition. *Scientific Reports*, 9(1), 1–12. <https://doi.org/10.1038/s41598-019-54023-2>
- Bagherpour, B., Bucher, H., Baud, A., Brosse, M., Vennemann, T., Martini, R., & Guodun, K. (2017). Onset, development, and cessation of basal early Triassic microbialites (BETM) in the Nanpanjiang pull-apart basin, South China Block. *Gondwana Research*, 44, 178–204. <https://doi.org/10.1016/j.gr.2016.11.013>
- Bagherpour, B., Bucher, H., Vennemann, T., Schneebeli-Hermann, E., Yuan, D. X., Leu, M., et al. (2020). Are Late Permian carbon isotope excursions of local or of global significance? *Geological Society of America Bulletin*, 132(3–4), 521–544. <https://doi.org/10.1130/B31996.1>
- Baresel, B., Bucher, H., Bagherpour, B., Brosse, M., Guodun, K., & Schaltegger, U. (2017). Timing of global regression and microbial bloom linked with the Permian-Triassic boundary mass extinction: Implications for driving mechanisms. *Scientific Reports*, 7(1), 43630. <https://doi.org/10.1038/srep43630>
- Baresel, B., Bucher, H., Brosse, M., Cordey, F., Kuang, G. D., & Schaltegger, U. (2017). Precise age for the Permian-Triassic boundary in South China from high-precision U-Pb geochronology and Bayesian age-depth modeling. *Solid Earth*, 8(2), 361–378. <https://doi.org/10.5194/se-8-361-2017>

- Baud, A., Atudorei, V., & Sharp, Z. (1996). Late Permian and Early Triassic evolution of the Northern Indian margin: Carbon isotope and sequence stratigraphy. *Geodinamica Acta*, 9(2–3), 57–77. <https://doi.org/10.1080/0985311.1996.11105278>
- Baud, A., Magaritz, M., & Holser, W. T. (1989). Permian-Triassic of the Tethys: Carbon isotope studies. *Geologische Rundschau*, 78(2), 649–677. <https://doi.org/10.1007/BF01776196>
- Behar, F., Beaumont, V., & Penteado, H. L. D. (2001). Rock-Eval 6 technology: Performances and developments. *Oil & Gas Science and Technology-Revue D Ifp Energies Nouvelles*, 56(2), 111–134. <https://doi.org/10.2516/ogst.2001013>
- Bergquist, B. A., & Blum, J. D. (2007). Mass-dependent and -independent fractionation of Hg isotopes by photoreduction in aquatic systems. *Science*, 318(5849), 417–420. <https://doi.org/10.1126/science.1148050>
- Black, B. A., Elkins-Tanton, L. T., Rowe, M. C., & Peate, I. U. (2012). Magnitude and consequences of volatile release from the Siberian Traps. *Earth and Planetary Science Letters*, 317, 363–373. <https://doi.org/10.1016/j.epsl.2011.12.001>
- Blum, J. D., & Bergquist, B. A. (2007). Reporting of variations in the natural isotopic composition of mercury. *Analytical and Bioanalytical Chemistry*, 388(2), 353–359. <https://doi.org/10.1007/s00216-007-1236-9>
- Blum, J. D., Sherman, L. S., & Johnson, M. W. (2014). Mercury isotopes in earth and environmental Sciences. *Annual Review of Earth and Planetary Sciences*, 42(42), 249–269. <https://doi.org/10.1146/annurev-earth-050212-124107>
- Bowring, J. F., McLean, N. M., & Bowring, S. A. (2011). Engineering cyber infrastructure for U-Pb geochronology: Tripoli and U-Pb_Redux. *Geochemistry, Geophysics, Geosystems*, 12(6), 19. <https://doi.org/10.1029/2010gc003479>
- Broadley, M. W., Barry, P. H., Ballentine, C. J., Taylor, L. A., & Burgess, R. (2018). End-Permian extinction amplified by plume-induced release of recycled lithospheric volatiles. *Nature Geoscience*, 11(9), 682–687. <https://doi.org/10.1038/s41561-018-0215-4>
- Brosse, M., Bucher, H., & Goudemand, N. (2016). Quantitative biochronology of the Permian-Triassic boundary in South China based on conodont unitary associations. *Earth-Science Reviews*, 155, 153–171. <https://doi.org/10.1016/j.earscirev.2016.02.003>
- Burgess, S. D., Bowring, S., & Shen, S. Z. (2014). High-precision timeline for Earth's most severe extinction. *Proceedings of the National Academy of Sciences*, 111(9), 3316–3321. <https://doi.org/10.1073/pnas.1317692111>
- Burgess, S. D., & Bowring, S. A. (2015). High-precision geochronology confirms voluminous magmatism before, during, and after Earth's most severe extinction. *Science Advances*, 1(7), e1500470. <https://doi.org/10.1126/sciadv.1500470>
- Burgess, S. D., Muirhead, J. D., & Bowring, S. A. (2017). Initial pulse of Siberian Traps sills as the trigger of the end-Permian mass extinction. *Nature Communications*, 8(1), 164. <https://doi.org/10.1038/s41467-017-00083-9>
- Callegaro, S., Svensen, H. H., Neumann, E. R., Polozov, A., Jerram, D. A., Deegan, F., et al. (2021). Geochemistry of deep Tunguska Basin sills, Siberian traps: Correlations and potential implications for the end-Permian environmental crisis. *Contributions to Mineralogy and Petrology*, 176(7), 1–30. <https://doi.org/10.1007/s00410-021-01807-3>
- Cao, C., Wang, W., & Jin, Y. (2002). Carbon isotope excursions across the Permian-Triassic boundary in the Meishan section, Zhejiang Province, China. *Chinese Science Bulletin*, 47(13), 1125–1129. <https://doi.org/10.1360/02tb9252>
- Caswell, T. A., Droettboom, M., Lee, A., Sales De Andrade, E., Hoffmann, T., Klymak, J., et al. (2022). Matplotlib v3.5.2 [Software]. Zenodo. <http://doi.org/10.5281/zenodo.6513224>
- Chapman, T., Milan, L. A., Metcalfe, I., Blevin, P. L., & Crowley, J. (2022). Pulses in silicic arc magmatism initiate end-Permian climate instability and extinction. *Nature Geoscience*, 15(5), 411–416. <https://doi.org/10.1038/s41561-022-00934-1>
- Charbonnier, G., Adatte, T., Föllmi, K. B., & Suan, G. (2020). Effect of intense weathering and Postdepositional degradation of organic matter on Hg/TOC proxy in organic-rich sediments and its implications for deep-time investigations. *Geochemistry, Geophysics, Geosystems*, 21(2), e2019GC008707. <https://doi.org/10.1029/2019GC008707>
- Charbonnier, G., Morales, C., Duchamp-Alphonse, S., Westermann, S., Adatte, T., & Föllmi, K. B. (2017). Mercury enrichment indicates volcanic triggering of Valanginian environmental change. *Scientific Reports*, 7(1), 1–6. <https://doi.org/10.1038/srep40808>
- Chen, D., Ren, D., Deng, C., Tian, Z., & Yin, R. (2022). Mercury loss and isotope fractionation during high-pressure and high-temperature processing of sediments: Implication for the behaviors of mercury during metamorphism. *Geochimica et Cosmochimica Acta*, 334, 231–240. <https://doi.org/10.1016/j.gca.2022.08.010>
- Chen, J., Hintelmann, H., Feng, X., & Dimock, B. (2012). Unusual fractionation of both odd and even mercury isotopes in precipitation from Peterborough, ON, Canada. *Geochimica et Cosmochimica Acta*, 90, 33–46. <https://doi.org/10.1016/j.gca.2012.05.005>
- Condon, D. J., Schoene, B., McLean, N. M., Bowring, S. A., & Parrish, R. R. (2015). Metrology and traceability of U-Pb isotope dilution geochronology (EARTHTIME Tracer Calibration Part I). *Geochimica et Cosmochimica Acta*, 164, 464–480. <https://doi.org/10.1016/j.gca.2015.05.026>
- Dai, X., Song, H., Brayard, A., & Ware, D. (2019). A new Griesbachian-Dienerian (induan, early Triassic) ammonoid fauna from Gujiao, south China. *Journal of Paleontology*, 93(1), 48–71. <https://doi.org/10.1017/jpa.2018.46>
- Dal Corso, J., Song, H., Callegaro, S., Chu, D., Sun, Y., Hilton, J., et al. (2022). Environmental crises at the Permian–Triassic mass extinction. *Nature Reviews Earth & Environment*, 3(3), 197–214. <https://doi.org/10.1038/s43017-021-00259-4>
- Davydov, V. (2021). Tunguska coals, Siberian sills and the Permian-Triassic extinction. *Earth-Science Reviews*, 212, 103438. <https://doi.org/10.1016/j.earscirev.2020.103438>
- Edward, O., Paul, A. N., Bucher, H., Vêrard, C., Adatte, T., Sonke, J. E., & Vennemann, T. (2023). Timing and provenance of volcanic fluxes around the Permian-Triassic boundary mass extinction in South China: U-Pb zircon geochronology, volcanic ash geochemistry and mercury isotopes [Dataset]. Zenodo. <http://doi.org/10.5281/zenodo.7972240>
- Ellwood, B. B., Wardlaw, B. R., Nestell, M. K., Nestell, G. P., & Lan, L. T. P. (2017). Identifying globally synchronous Permian–Triassic boundary levels in successions in China and Vietnam using Graphic Correlation. *Palaeogeography, Palaeoclimatology, Palaeoecology*, 485, 561–571. <https://doi.org/10.1016/j.palaeo.2017.07.012>
- Erwin, D. H. (1998). The end and the beginning: Recoveries from mass extinctions. *Trends in Ecology & Evolution*, 13(9), 344–349. [https://doi.org/10.1016/S0169-5347\(98\)01436-0](https://doi.org/10.1016/S0169-5347(98)01436-0)
- Espitalié, J., Deroo, G., & Marquis, F. (1985). La pyrolyse Rock-Eval et ses applications. *Revue de l'Institut Français du Pétrole*, 40(5), 563–579. <https://doi.org/10.2516/ogst.1985035>
- Fantasia, A., Föllmi, K. B., Adatte, T., Bernárdez, E., Spangenberg, J. E., & Mattioli, E. (2018). The Toarcian oceanic anoxic event in southwestern Gondwana: An example from the Andean basin, northern Chile. *Journal of the Geological Society*, 175(6), 883–902. <https://doi.org/10.1144/jgs2018-008>
- Fendley, I. M., Mittal, T., Sprain, C. J., Marvin-DiPasquale, M., Tobin, T. S., & Renne, P. R. (2019). Constraints on the volume and rate of Deccan Traps flood basalt eruptions using a combination of high-resolution terrestrial mercury records and geochemical box models. *Earth and Planetary Science Letters*, 524, 115721. <https://doi.org/10.1016/j.epsl.2019.115721>
- Font, E., Chen, J., Regelous, M., Regelous, A., & Adatte, T. (2021). Volcanic origin of the mercury anomalies at the Cretaceous-Paleogene transition of Bidart. *France. Geology*, 50(2), 142–146. <https://doi.org/10.1130/G49458.1>

- Fu, X., Jiskra, M., Yang, X., Maruszczak, N., Enrico, M., Chmeleff, J., et al. (2021). Mass-independent fractionation of even and odd mercury isotopes during atmospheric mercury redox reactions. *Environmental Science & Technology*, 55(14), 10164–10174. <https://doi.org/10.1021/acs.est.1c02568>
- Gao, Q., Zhang, N., Xia, W., Feng, Q., Chen, Z.-Q., Zheng, J., et al. (2013). Origin of volcanic ash beds across the Permian–Triassic boundary, Daxiakou, South China: Petrology and U–Pb age, trace elements and Hf-isotope composition of zircon. *Chemical Geology*, 360, 41–53. <https://doi.org/10.1016/j.chemgeo.2013.09.020>
- Gastaldo, R. A., Kamo, S. L., Neveling, J., Geissman, J. W., Looy, C. V., & Martini, A. M. (2020). The base of the Lystrosaurus Assemblage Zone, Karoo Basin, predates the end-Permian marine extinction. *Nature Communications*, 11(1), 1–8. <https://doi.org/10.1038/s41467-020-15243-7>
- Grasby, S. E., Beauchamp, B., Bond, D. P., Wignall, P. B., & Sanei, H. (2016). Mercury anomalies associated with three extinction events (Capitanian crisis, latest Permian extinction and the Smithian/Spathian extinction) in NW Pangea. *Geological Magazine*, 153(2), 285–297. <https://doi.org/10.1017/s0016756815000436>
- Grasby, S. E., Sanei, H., & Beauchamp, B. (2011). Catastrophic dispersion of coal fly ash into oceans during the latest Permian extinction. *Nature Geoscience*, 4(2), 104–107. <https://doi.org/10.1038/ngeo1069>
- Grasby, S. E., Sanei, H., Beauchamp, B., & Chen, Z. H. (2013). Mercury deposition through the Permo-Triassic biotic crisis. *Chemical Geology*, 351, 209–216. <https://doi.org/10.1016/j.chemgeo.2013.05.022>
- Grasby, S. E., Shen, W. J., Yin, R. S., Gleason, J. D., Blum, J. D., Lepak, R. F., et al. (2017). Isotopic signatures of mercury contamination in latest Permian oceans. *Geology*, 45(1), 55–58. <https://doi.org/10.1130/G38487.1>
- Grasby, S. E., Them, T. R., Chen, Z. H., Yin, R. S., & Ardakani, O. H. (2019). Mercury as a proxy for volcanic emissions in the geologic record. *Earth-Science Reviews*, 196, 102880. <https://doi.org/10.1016/j.earscirev.2019.102880>
- Guex, J. (1991). *Biochronological correlations* (1 ed., Vol. 250). Springer.
- Hardisty, D. S., Lyons, T. W., Riedinger, N., Isson, T. T., Owens, J. D., Aller, R. C., et al. (2018). An evaluation of sedimentary molybdenum and iron as proxies for pore fluid paleoredox conditions. *American Journal of Science*, 318(5), 527–556. <https://doi.org/10.2475/05.2018.04>
- He, B., Zhong, Y. T., Xu, Y. G., & Li, X. H. (2014). Triggers of Permo-Triassic boundary mass extinction in South China: The Siberian traps or paleo-Tethys ignimbrite flare-up? *Lithos*, 204, 258–267. <https://doi.org/10.1016/j.lithos.2014.05.011>
- Holland, S. M., & Patzkowsky, M. E. (2015). The stratigraphy of mass extinction. *Palaeontology*, 58(5), 903–924. <https://doi.org/10.1111/pala.12188>
- Huang, H., Huyskens, M. H., Yin, Q.-Z., Cawood, P. A., Hou, M., Yang, J., et al. (2022). Eruptive tempo of Emeishan large igneous province, southwestern China and northern Vietnam: Relations to biotic crises and paleoclimate changes around the Guadalupian-Lopingian boundary. *Geology*, 50(9), 1083–1087. <https://doi.org/10.1130/G50183.1>
- Jiao, Y., Zhou, L., Algeo, T. J., Shen, J., Feng, L., Hu, Y., et al. (2022). Zirconium isotopes track volcanic inputs during the Permian-Triassic transition in South China. *Chemical Geology*, 610, 121074. <https://doi.org/10.1016/j.chemgeo.2022.121074>
- Jiskra, M., Heimburger-Boavida, L. E., Desgranges, M. M., Petrova, M. V., Dufour, A., Ferreira-Araujo, B., et al. (2021). Mercury stable isotopes constrain atmospheric sources to the ocean. *Nature*, 597(7878), 678–682. <https://doi.org/10.1038/s41586-021-03859-8>
- Jiskra, M., Sonke, J. E., Agnan, Y., Helmig, D., & Obrist, D. (2019). Insights from mercury stable isotopes on terrestrial-atmosphere exchange of Hg(0) in the Arctic tundra. *Biogeosciences*, 16(20), 4051–4064. <https://doi.org/10.5194/bg-16-4051-2019>
- Joachimski, M. M., Lai, X., Shen, S., Jiang, H., Luo, G., Chen, B., et al. (2012). Climate warming in the latest Permian and the Permian–Triassic mass extinction. *Geology*, 40(3), 195–198. <https://doi.org/10.1130/G32707.1>
- Johnson, D. L., Present, T. M., Li, M., Shen, Y., & Adkins, J. F. (2021). Carbonate associated sulfate (CAS) $\delta^{34}\text{S}$ heterogeneity across the end-Permian mass extinction in South China. *Earth and Planetary Science Letters*, 574, 117172. <https://doi.org/10.1016/j.epsl.2021.117172>
- Korte, C., & Kozur, H. W. (2010). Carbon-isotope stratigraphy across the Permian-Triassic boundary: A review. *Journal of Asian Earth Sciences*, 39(4), 215–235. <https://doi.org/10.1016/j.jseas.2010.01.005>
- Kwon, S. Y., Blum, J. D., Nadelhoffer, K. J., Dvonch, J. T., & Tsui, M. T.-K. (2015). Isotopic study of mercury sources and transfer between a freshwater lake and adjacent forest food web. *Science of the Total Environment*, 532, 220–229. <https://doi.org/10.1016/j.scitotenv.2015.06.012>
- Lehrmann, D. J., Stepchinski, L., Altiner, D., Orchard, M. J., Montgomery, P., Enos, P., et al. (2015). An integrated biostratigraphy (conodonts and foraminifers) and chronostratigraphy (paleomagnetic reversals, magnetic susceptibility, elemental chemistry, carbon isotopes and geochronology) for the Permian–Upper Triassic strata of Guandao section, Nanpanjiang Basin, south China. *Journal of Asian Earth Sciences*, 108, 117–135. <https://doi.org/10.1016/j.jseas.2015.04.030>
- Leu, M., Bucher, H., & Goudemand, N. (2019). Clade-dependent size response of conodonts to environmental changes during the late Smithian extinction. *Earth-Science Reviews*, 195, 52–67. <https://doi.org/10.1016/j.earscirev.2018.11.003>
- Leu, M., Bucher, H., Vennemann, T., Bagherpour, B., Ji, C., Brosse, M., & Goudemand, N. (2022). A unitary association-based conodont biozonation of the Smithian–Spathian boundary (early Triassic) and associated biotic crisis from South China. *Swiss Journal of Palaeontology*, 141(1), 19. <https://doi.org/10.1186/s13358-022-00259-x>
- Liu, Z., Percival, L. M. E., Vandeputte, D., Selby, D., Claeys, P., Over, D. J., & Gao, Y. (2021). Upper Devonian mercury record from North America and its implications for the Frasnian–Famennian mass extinction. *Palaeogeography, Palaeoclimatology, Palaeoecology*, 576, 110502. <https://doi.org/10.1016/j.palaeo.2021.110502>
- Luppo, T., de Luchi, M. G. L., Rapalini, A. E., Dopico, C. I. M., & Fanning, C. M. (2018). Geochronologic evidence of a large magmatic province in northern Patagonia encompassing the Permian-Triassic boundary. *Journal of South American Earth Sciences*, 82, 346–355. <https://doi.org/10.1016/j.jsames.2018.01.003>
- McLean, N. M., Bowring, J. F., & Bowring, S. A. (2011). An algorithm for U–Pb isotope dilution data reduction and uncertainty propagation. *Geochemistry, Geophysics, Geosystems*, 12(6), Q0AA18. <https://doi.org/10.1029/2010GC003478>
- Metcalfe, I., Crowley, J., Nicoll, R., & Schmitz, M. (2015). High-precision U–Pb CA-TIMS calibration of Middle Permian to Lower Triassic sequences, mass extinction and extreme climate-change in eastern Australian Gondwana. *Gondwana Research*, 28(1), 61–81. <https://doi.org/10.1016/j.gr.2014.09.002>
- Moynier, F., Jackson, M. G., Zhang, K., Cai, H., Halldörsson, S. A., Pik, R., et al. (2021). The mercury isotopic composition of Earth's Mantle and the use of mass independently fractionated Hg to test for recycled crust. *Geophysical Research Letters*, 48(17), e2021GL094301. <https://doi.org/10.1029/2021GL094301>
- Nelson, D. A., & Cottle, J. M. (2019). Tracking voluminous permian volcanism of the choiyo province into central Antarctica. *Lithosphere*, 11(3), 386–398. <https://doi.org/10.1130/1015.1>
- Payne, J. L., & Kump, L. R. (2007). Evidence for recurrent Early Triassic massive volcanism from quantitative interpretation of carbon isotope fluctuations. *Earth and Planetary Science Letters*, 256(1–2), 264–277. <https://doi.org/10.1016/j.epsl.2007.01.034>
- Pearce, J. A. (1982). Trace element characteristics of lavas from destructive plate boundaries. In R. S. Thorpe (Ed.), *Orogenic andesites and related rocks* (pp. 528–548). John Wiley and Sons.

- Pearce, J. A., Baker, P. E., Harvey, P. K., & Luff, I. W. (1995). Geochemical evidence for subduction fluxes, mantle melting and fractional crystallization beneath the South Sandwich island arc. *Journal of Petrology*, *36*(4), 1073–1109. <https://doi.org/10.1093/ptrology/36.4.1073>
- Percival, L. M. E., Bergquist, B. A., Mather, T. A., & Sanei, H. (2021). Sedimentary mercury enrichments as a tracer of large igneous province volcanism. In R. E. Ernst, A. J. Dickson, & A. Bekker (Eds.), *Large Igneous Provinces* (pp. 247–262). John Wiley and Sons, Inc.
- Percival, L. M. E., Jenkyns, H. C., Mather, T. A., Dickson, A. J., Batenburg, S. J., Ruhl, M., et al. (2018). Does large igneous province volcanism always perturb the mercury cycle? Comparing the records of oceanic anoxic event 2 and the end-cretaceous to other mesozoic events. *American Journal of Science*, *318*(8), 799–860. <https://doi.org/10.2475/08.2018.01>
- Portnyagin, M. V., Ponomareva, V. V., Zelenin, E. A., Bazanova, L. I., Pevzner, M. M., Plechova, A. A., et al. (2020). TephraKam: Geochemical database of glass compositions in tephra and welded tuffs from the kamchatka volcanic arc (northwestern Pacific). *Earth System Science Data*, *12*(1), 469–486. <https://doi.org/10.5194/essd-12-469-2020>
- Pyle, D. M., & Mather, T. A. (2003). The importance of volcanic emissions for the global atmospheric mercury cycle. *Atmospheric Environment*, *37*(36), 5115–5124. <https://doi.org/10.1016/j.atmosenv.2003.07.011>
- Racki, G. (2020). A volcanic scenario for the Frasnian–Famennian major biotic crisis and other Late Devonian global changes: More answers than questions? *Global and Planetary Change*, *189*, 103174. <https://doi.org/10.1016/j.gloplacha.2020.103174>
- Reichow, M. K., Saunders, A. D., White, R. V., Al'Mukhamedov, A. I., & Medvedev, A. Y. (2005). Geochemistry and petrogenesis of basalts from the west Siberian basin: An extension of the Permo–Triassic Siberian traps, Russia. *Lithos*, *79*(3), 425–452. <https://doi.org/10.1016/j.lithos.2004.09.011>
- Rolison, J. M., Stirling, C. H., Middag, R., & Rijkenberg, M. J. A. (2017). Uranium stable isotope fractionation in the Black Sea: Modern calibration of the $^{238}\text{U}/^{235}\text{U}$ paleo-redox proxy. *Geochimica et Cosmochimica Acta*, *203*, 69–88. <https://doi.org/10.1016/j.gca.2016.12.014>
- Saccani, E., Delavari, M., Dolati, A., Marroni, M., Pandolfi, L., Chiari, M., & Barbero, E. (2018). New insights into the geodynamics of Neo-Tethys in the Makran area: Evidence from age and petrology of ophiolites from the Coloured Mélange Complex (SE Iran). *Gondwana Research*, *62*, 306–327. <https://doi.org/10.1016/j.gr.2017.07.013>
- Saccani, E., Dilek, Y., Marroni, M., & Pandolfi, L. (2015). Continental margin ophiolites of Neotethys: Remnants of ancient ocean–continent transition zone (OCTZ) lithosphere and their geochemistry, mantle sources and melt evolution patterns. *Episodes Journal of International Geoscience*, *38*(4), 230–249. <https://doi.org/10.18814/epiugs/2015/v38i4/82418>
- Sanei, H., Grasby, S. E., & Beauchamp, B. (2012). Latest Permian mercury anomalies. *Geology*, *40*(1), 63–66. <https://doi.org/10.1130/G32596.1>
- Schaltegger, U., Ovtcharova, M., Gaynor, S. P., Schoene, B., Wotzlaw, J.-F., Davies, J. F., et al. (2021). Long-term repeatability and interlaboratory reproducibility of high-precision ID-TIMS U–Pb geochronology. *Journal of Analytical Atomic Spectrometry*, *36*(7), 1466–1477. <https://doi.org/10.1039/D1JA00116G>
- Schoene, B., Crowley, J. L., Condon, D. J., Schmitz, M. D., & Bowring, S. A. (2006). Reassessing the uranium decay constants for geochronology using ID-TIMS U–Pb data. *Geochimica et Cosmochimica Acta*, *70*(2), 426–445. <https://doi.org/10.1016/j.gca.2005.09.007>
- Shen, J., Algeo, T. J., Hu, Q., Xu, G., Zhou, L., & Feng, Q. (2013). Volcanism in South China during the Late Permian and its relationship to marine ecosystem and environmental changes. *Global and Planetary Change*, *105*, 121–134. <https://doi.org/10.1016/j.gloplacha.2012.02.011>
- Shen, J., Chen, J., Algeo, T. J., Feng, Q., Yu, J., Xu, Y.-G., et al. (2021). Mercury fluxes record regional volcanism in the South China craton prior to the end-Permian mass extinction. *Geology*, *49*(4), 452–456. <https://doi.org/10.1130/G48501.1>
- Shen, J., Chen, J., Algeo, T. J., Yuan, S., Feng, Q., Yu, J., et al. (2019). Evidence for a prolonged Permian–Triassic extinction interval from global marine mercury records. *Nature Communications*, *10*(1), 1563. <https://doi.org/10.1038/s41467-019-09620-0>
- Shen, J., Chen, J., Yu, J., Algeo, T. J., Smith, R. M. H., Botha, J., et al. (2023). Mercury evidence from southern Pangea terrestrial sections for end-Permian global volcanic effects. *Nature Communications*, *14*(1), 6. <https://doi.org/10.1038/s41467-022-35272-8>
- Shen, J., Feng, Q. L., Algeo, T. J., Liu, J. L., Zhou, C. Y., Wei, W., et al. (2020). Sedimentary host phases of mercury (Hg) and implications for use of Hg as a volcanic proxy. *Earth and Planetary Science Letters*, *543*, 116333. <https://doi.org/10.1016/j.epsl.2020.116333>
- Shen, S.-Z., Cao, C.-Q., Zhang, H., Bowring, S. A., Henderson, C. M., Payne, J. L., et al. (2013). High-resolution $\delta^{13}\text{C}$ carb chemostratigraphy from latest Guadalupian through earliest Triassic in South China and Iran. *Earth and Planetary Science Letters*, *375*, 156–165. <https://doi.org/10.1016/j.epsl.2013.05.020>
- Shen, S. Z., Crowley, J. L., Wang, Y., Bowring, S. A., Erwin, D. H., Sadler, P. M., et al. (2011). Calibrating the end-Permian mass extinction. *Science*, *334*(6061), 1367–1372. <https://doi.org/10.1126/science.1213454>
- Shen, S. Z., Ramezani, J., Chen, J., Cao, C. Q., Erwin, D. H., Zhang, H., et al. (2019). A sudden end-Permian mass extinction in South China. *Geological Society of America Bulletin*, *131*(1–2), 205–223. <https://doi.org/10.1130/B31909.1>
- Sial, A. N., Chen, J. B., Lacerda, L. D., Korte, C., Spangenberg, J. E., Silva-Tamayo, J. C., et al. (2020). Globally enhanced Hg deposition and Hg isotopes in sections straddling the Permian–Triassic boundary: Link to volcanism. *Palaeogeography, Palaeoclimatology, Palaeoecology*, *540*, 109537. <https://doi.org/10.1016/j.palaeo.2019.109537>
- Sibik, S., Edmonds, M., MacLennan, J., & Svensen, H. (2015). Magmas erupted during the main pulse of Siberian Traps volcanism were volatile-poor. *Journal of Petrology*, *56*(11), 2089–2116. <https://doi.org/10.1093/ptrology/egv064>
- Sibik, S., Edmonds, M., Villemant, B., Svensen, H. H., Polozov, A. G., & Planke, S. (2021). Halogen enrichment of Siberian Traps magmas during interaction with evaporites. <https://doi.org/10.3389/feart.2021.741447>
- Sobolev, A. V., Krivolutsкая, N. A., & Kuzmin, D. V. (2009). Petrology of the parental melts and mantle sources of Siberian trap magmatism. *Petrology*, *17*(3), 253–286. <https://doi.org/10.1134/S0869591109030047>
- Song, H., Wignall, P. B., Tong, J., & Yin, H. (2013). Two pulses of extinction during the Permian–Triassic crisis. *Nature Geoscience*, *6*(1), 52–56. <https://doi.org/10.1038/ngeo1649>
- Song, Q., Hong, H., Algeo, T. J., Fang, Q., Zhao, C., Liu, C., & Xu, Y. (2022). Clay mineralogy mediated by pH and chemical weathering intensity of Permian–Triassic boundary K-bentonites at Dongpan (Guangxi, South China). *Chemical Geology*, *617*, 121262. <https://doi.org/10.1016/j.chemgeo.2022.121262>
- Sonke, J. E., Schafer, J., Chmeleff, J., Audry, S., Blanc, G., & Dupre, B. (2010). Sedimentary mercury stable isotope records of atmospheric and riverine pollution from two major European heavy metal refineries. *Chemical Geology*, *279*(3–4), 90–100. <https://doi.org/10.1016/j.chemgeo.2010.09.017>
- Stanley, S. M. (2016). Estimates of the magnitudes of major marine mass extinctions in Earth history. *Proceedings of the National Academy of Sciences*, *113*(42), E6325–E6334. <https://doi.org/10.1073/pnas.1613094113>
- Sun, R., Enrico, M., Heimburger, L. E., Scott, C., & Sonke, J. E. (2013). A double-stage tube furnace—Acid-trapping protocol for the pre-concentration of mercury from solid samples for isotopic analysis. *Analytical and Bioanalytical Chemistry*, *405*(21), 6771–6781. <https://doi.org/10.1007/s00216-013-7152-2>
- Sun, S.-S., & McDonough, W. F. (1989). Chemical and isotopic systematics of oceanic basalts: Implications for mantle composition and processes. *Geological Society, London, Special Publications*, *42*(1), 313–345. <https://doi.org/10.1144/GSL.SP.1989.042.01.1>

- Svensen, H., Planke, S., Polozov, A. G., Schmidbauer, N., Corfu, F., Podladchikov, Y. Y., & Jamtveit, B. (2009). Siberian gas venting and the end-Permian environmental crisis. *Earth and Planetary Science Letters*, 277(3–4), 490–500. <https://doi.org/10.1016/j.epsl.2008.11.015>
- Svensen, H. H., Frolov, S., Akhmanov, G. G., Polozov, A. G., Jerram, D. A., Shiganova, O. V., et al. (2018). Sills and gas generation in the Siberian traps. *Philosophical Transactions of the Royal Society A*, 376(2130), 20170080. <https://doi.org/10.1098/rsta.2017.0080>
- Them, T., II, Jagoe, C., Caruthers, A., Gill, B., Grasby, S., Gröcke, D., et al. (2019). Terrestrial sources as the primary delivery mechanism of mercury to the oceans across the Toarcian oceanic anoxic event (early Jurassic). *Earth and Planetary Science Letters*, 507, 62–72. <https://doi.org/10.1016/j.epsl.2018.11.029>
- Thibodeau, A. M., & Bergquist, B. A. (2017). Do mercury isotopes record the signature of massive volcanism in marine sedimentary records? *Geology*, 45(1), 95–96. <https://doi.org/10.1130/focus012017.1>
- Thibodeau, A. M., Ritterbush, K., Yager, J. A., West, A. J., Ibarra, Y., Bottjer, D. J., et al. (2016). Mercury anomalies and the timing of biotic recovery following the end-Triassic mass extinction. *Nature Communications*, 7(1), 11147. <https://doi.org/10.1038/ncomms11147>
- Tribouillard, N., Algeo, T. J., Lyons, T., & Riboulleau, A. (2006). Trace metals as paleoredox and paleoproductivity proxies: An update. *Chemical Geology*, 232(1–2), 12–32. <https://doi.org/10.1016/j.chemgeo.2006.02.012>
- Vajda, V., McLoughlin, S., Mays, C., Frank, T. D., Fielding, C. R., Tevyaw, A., et al. (2020). End-permian (252 mya) deforestation, wildfires and flooding—An ancient biotic crisis with lessons for the present. *Earth and Planetary Science Letters*, 529, 115875. <https://doi.org/10.1016/j.epsl.2019.115875>
- Vérard, C. (2019). Panalexis: Towards global synthetic palaeogeographies using integration and coupling of manifold models. *Geological Magazine*, 156(2), 320–330. <https://doi.org/10.1017/S0016756817001042>
- Vérard, C., Hochard, C., Baumgartner, P. O., Stampfli, G. M., & Liu, M. (2015a). 3D palaeogeographic reconstructions of the Phanerozoic versus sea-level and Sr-ratio variations. *Journal of Palaeogeography*, 4(1), 64–84. <https://doi.org/10.3724/SP.J.1261.2015.00068>
- Vérard, C., Hochard, C., Baumgartner, P. O., Stampfli, G. M., & Liu, M. (2015b). Geodynamic evolution of the Earth over the Phanerozoic: Plate tectonic activity and palaeoclimatic indicators. *Journal of Palaeogeography*, 4(2), 167–188. <https://doi.org/10.3724/SP.J.1261.2015.00072>
- Wang, X., Cawood, P. A., Zhao, H., Zhao, L., Grasby, S. E., Chen, Z.-Q., & Zhang, L. (2019). Global mercury cycle during the end-Permian mass extinction and subsequent Early Triassic recovery. *Earth and Planetary Science Letters*, 513, 144–155. <https://doi.org/10.1016/j.epsl.2019.02.026>
- Wang, X., Cawood, P. A., Zhao, L., Chen, Z.-Q., Lyu, Z., & Ma, B. (2019). Convergent continental margin volcanic source for ash beds at the Permian-Triassic boundary, South China: Constraints from trace elements and Hf-isotopes. *Palaeogeography, Palaeoclimatology, Palaeoecology*, 519, 154–165. <https://doi.org/10.1016/j.palaeo.2018.02.011>
- Wang, X. D., Cawood, P. A., Zhao, H., Zhao, L. S., Grasby, S. E., Chen, Z. Q., et al. (2018). Mercury anomalies across the end Permian mass extinction in South China from shallow and deep water depositional environments. *Earth and Planetary Science Letters*, 496, 159–167. <https://doi.org/10.1016/j.epsl.2018.05.044>
- Waskom, M. L. (2021). Seaborn: Statistical data visualization [Software]. *Journal of Open Source Software*, 6(60), 3021. <https://doi.org/10.21105/joss.03021>
- Widmann, P., Bucher, H., Leu, M., Vennemann, T., Bagherpour, B., Schneebeil-Hermann, E., et al. (2020). Dynamics of the largest carbon isotope excursion during the Early Triassic biotic recovery. *Front Earth Sc-Switz*, 8, 196. <https://doi.org/10.3389/feart.2020.00196>
- Widmann, P., Davies, J. H. F. L., & Schaltegger, U. (2019). Calibrating chemical abrasion: Its effects on zircon crystal structure, chemical composition and U Pb age. *Chemical Geology*, 511, 1–10. <https://doi.org/10.1016/j.chemgeo.2019.02.026>
- Wignall, P. B., Morante, R., & Newton, R. (1998). The Permo-Triassic transition in Spitsbergen: $\delta^{13}\text{C}_{\text{org}}$ chemostratigraphy, Fe and S geochemistry, facies, fauna and trace fossils. *Geological Magazine*, 135(1), 47–62. <https://doi.org/10.1017/S0016756897008121>
- Winchester, J. A., & Floyd, P. A. (1977). Geochemical discrimination of different magma series and their differentiation products using immobile elements. *Chemical Geology*, 20, 325–343. [https://doi.org/10.1016/0009-2541\(77\)90057-2](https://doi.org/10.1016/0009-2541(77)90057-2)
- Yager, J. A., West, A. J., Thibodeau, A. M., Corsetti, F. A., Rigo, M., Berelson, W. M., et al. (2021). Mercury contents and isotope ratios from diverse depositional environments across the Triassic-Jurassic Boundary: Towards a more robust mercury proxy for large igneous province magmatism. *Earth-Science Reviews*, 223, 103775. <https://doi.org/10.1016/j.earscirev.2021.103775>
- Yang, J., Cawood, P. A., Du, Y., Huang, H., Huang, H., & Tao, P. (2012). Large Igneous Province and magmatic arc sourced Permian–Triassic volcanogenic sediments in China. *Sedimentary Geology*, 261, 120–131. <https://doi.org/10.1016/j.sedgeo.2012.03.018>
- Yin, H., Jiang, H., Xia, W., Feng, Q., Zhang, N., & Shen, J. (2014). The end-Permian regression in South China and its implication on mass extinction. *Earth-Science Reviews*, 137, 19–33. <https://doi.org/10.1016/j.earscirev.2013.06.003>
- Yin, H., Siji, H., Kexing, Z., Hansen, H., Fengqing, Y., Meihua, D., & Xianmei, B. (1992). The effects of volcanism on the Permo-Triassic mass extinction in South China. In J. M. Dickins, W. C. Sweet, Y. Zunyi, & Y. Hongfu (Eds.), *Permo-triassic events in the eastern Tethys: Stratigraphy classification and relations with the Western Tethys* (pp. 146–157). Cambridge University Press.
- Yin, H., Zhang, K., Tong, J., Yang, Z., & Wu, S. (2001). The global stratotype section and point (GSSP) of the Permian-Triassic boundary. *Episodes*, 24(2), 102–114. <https://doi.org/10.18814/epiugs/2001/v24i2/004>
- Yin, R., Chen, D., Pan, X., Deng, C., Chen, L., Song, X., et al. (2022). Mantle Hg isotopic heterogeneity and evidence of oceanic Hg recycling into the mantle. *Nature Communications*, 13(1), 948. <https://doi.org/10.1038/s41467-022-28577-1>
- Yuan, D.-X., Shen, S.-Z., Henderson, C. M., Chen, J., Zhang, H., Zheng, Q.-F., & Wu, H. (2019). Integrative timescale for the Lopingian (Late Permian): A review and update from Shangsi, South China. *Earth-Science Reviews*, 188, 190–209. <https://doi.org/10.1016/j.earscirev.2018.11.002>
- Zambardi, T., Sonke, J. E., Toutain, J. P., Sortino, F., & Shinohara, H. (2009). Mercury emissions and stable isotopic compositions at Vulcano Island (Italy). *Earth and Planetary Science Letters*, 277(1–2), 236–243. <https://doi.org/10.1016/j.epsl.2008.10.023>
- Zhang, G. J., Zhang, X. L., & Shen, Y. N. (2021). Quantitative constraints on carbon cycling and temporal changes in episodic euxinia during the end-Permian mass extinction in South China. *Chemical Geology*, 562, 120036. <https://doi.org/10.1016/j.chemgeo.2020.120036>
- Zhang, H., Zhang, F., Chen, J. B., Erwin, D. H., Syverson, D. D., Ni, P., et al. (2021). Felsic volcanism as a factor driving the end-Permian mass extinction. *Science Advances*, 7(47), eabh1390. <https://doi.org/10.1126/sciadv.abh1390>
- Zhao, H., Shen, J., Algeo, T. J., Racki, G., Chen, J., Huang, C., et al. (2022). Mercury isotope evidence for regional volcanism during the Frasnian-Famennian transition. *Earth and Planetary Science Letters*, 581, 117412. <https://doi.org/10.1016/j.epsl.2022.117412>
- Zhao, T. Y., Algeo, T. J., Feng, Q. L., Zi, J. W., & Xu, G. Z. (2019). Tracing the provenance of volcanic ash in Permian-Triassic boundary strata, South China: Constraints from inherited and syn-depositional magmatic zircons. *Palaeogeography, Palaeoclimatology, Palaeoecology*, 516, 190–202. <https://doi.org/10.1016/j.palaeo.2018.12.002>

- Zheng, B. S., Mou, C. L., Zhou, R. J., Wang, X. P., Xiao, Z. H., & Chen, Y. (2020). Nature and origin of the volcanic ash beds near the Permian-Triassic boundary in South China: New data and their geological implications. *Geological Magazine*, 157(4), 677–689. <https://doi.org/10.1017/S001675681900133x>
- Zintwana, M. P., Cawthorn, R. G., Ashwal, L. D., Roelofse, F., & Cronwright, H. (2012). Mercury in the Bushveld complex, South Africa, and the Skaergaard intrusion, Greenland. *Chemical Geology*, 320, 147–155. <https://doi.org/10.1016/j.chemgeo.2012.06.001>